POLITECNICO DI TORINO

Master's Degree in Sustainable Nuclear Energy

Master's Thesis

Model planning for laser thermal therapies

Developments and optimization of thermal models for tumor laser ablation

Supervisors

Prof. Gianni Coppa

Prof. Guido Perrone

Dott. Aurora Bellone

Candidate

Fabio Trerè

Academic Year 2022/2023

Abstract

As the second greatest cause of mortality in USA, cancer is an important problem for global public health.

Significant reductions in mortality have been observed over the past ten years as a result of enhanced therapies, detection methods, and targeted treatment development. A variety of cancer treatments already exist which exploit various tactics and scientific concepts such as chemotherapy, radiation therapy, photodynamic therapy, hormone therapy, immunotherapy, stem cell therapy, and targeted therapy.

Most of them have been consolidated over the last few years; nevertheless, other therapies for curing liver and lung cancer, for example, are still unreliable and mostly, too invasive. Hence, a great interest has growth in minimally invasive treatments that aim to target metastases while causing the least amount of harm to the patients.

This thesis examined the process of laser ablation, in which cancerous cells are directly targeted with lasers to raise their temperature and induce necrosis. In fact, living cells can develop and survive in temperatures ranges between 30 and 40 °C, but they do not survive temperatures exceeding 60 °C.

Because fiber-optic biomedical laser applications have so many benefits over traditional ones, they have grown significantly in the last several years. Their resilience, compact dimensions, and high energy efficiency make them suitable for a wide range of biomedical applications. Their energy here is used to cause specific cells to necrotize, enabling accurate non-invasive treatments that benefit patients more.

This master's thesis sought to create a realistic thermal model that could simulate biological tissue interaction with a laser, its propagation range and the temperature rise it causes, to serve as a mock-up for medical personnel administering treatments.

To obtain the numerical solutions and compare them with the analytical ones, a model was first made up and implemented into Comsol Multiphysics.

Secondly, the heat pulse method was exploited to assess the model's thermal biological properties, which are crucial for determining the accurate heat distribution across the media under study.

Then, Matlab codes were used to extract temperature data in real time.

The distortion caused by the monitoring fibre over the measured temperature values was also a subject of investigation. As a result of this study, experimental tests employing fibre laser beam delivery and FBG sensors were required in order to validate the distortion temperature maps previously produced.

Lastly, an investigation on a more realistic delivery system was conducted. Therefore, the heat source was constructed as a linearly distributed superposition of various Gaussians, taking advantage of the linearity of the heat equation.

Acknowledgements

I feel humbled for having received such a special support from dear professors Gianni Coppa and Guido Perrone, who generously and patiently guided me along this thesis path. I deeply thank also dott. Aurora Bellone, who as well, has provided me with fundamental assistance.

This master path was longer and more complex than expected, but nonetheless worth. These years have changed me in many ways. Torino has provided me two new families. The university one, where I was lucky to find beautiful people like: Marika, Federica, Lorenzo, Pietro, Andrea, Davide, Michele, who had always my back during my ups and downs. I will always be grateful for that. Thank you. I found another family in theatre, my deepest passion. I sincerely thank all the people that I've encountered in this beautiful path, rich of craziness and passion. Finally, I express my gratitude to my brother Simone who has always represented more than just a brother, but also a dear friend, and to the rest of my family that have supported me despite my lack of consistency and the unexpected decision to switch my life-direction. I know that it must have been hard, but we have one life, and we must live it as happily as possible. My choices are tough, difficult, and for that I'm proud of myself, and to be a professional actor, a nuclear engineer, and mostly a friend. I would like to also thank my friends from Ravenna. We've been through a lot. I know I have not been present in the past few years, but that is how life goes, and I'm grateful for your support despite the kilometres that separated us.

Table of Contents

List of figures

List of tables

List of acronyms

CRC- Colorectal cancer

RFA- Radiofrequency ablation

MWA- Microwave ablation

LA- Laser ablation

HIFU- High-intensity focused ultrasound

UV- Ultraviolet

NIR- Near-infrared

MIR- Mid infrared. Continuous

CW- Continuous waves emitters

TIR- Total internal reflection

NA- Numerical aperture

LED- Light emitting diode

PDE- Partial differential equation

LASER- light amplification simulated emission

FEM- Finite element method

FBG- Fiber Brigg Gratings

PBHTE- Pennet’s bio-heat transfer equation

RTD- Resistance temperature detector

HPM- Heat pulse method

BC- Boundary condition

CPU- Central processing unit

Nd:YAG- Neodymium-doped yttrium aluminium garnet laser

WL- Wavelength

CM- Comsol Multiphysics

Chapter 1

Introduction

A group of diseases known as cancer are defined by the uncontrolled proliferation and dissemination of defective cells, which, if left untreated, can be lethal.

Cancers may arise practically anywhere in the human body when aberrant or damaged cells interfere with a normal cell's ability to develop and reproduce. Tumours are lumps of tissue that can be formed by these cells. They may be benign or cancerous.

When the formers spread, a process known as metastasis occurs, in which malignant cells invade surrounding tissues. Contrarily, benign tumours do not grow back after removal and do not spread to neighbouring tissues.

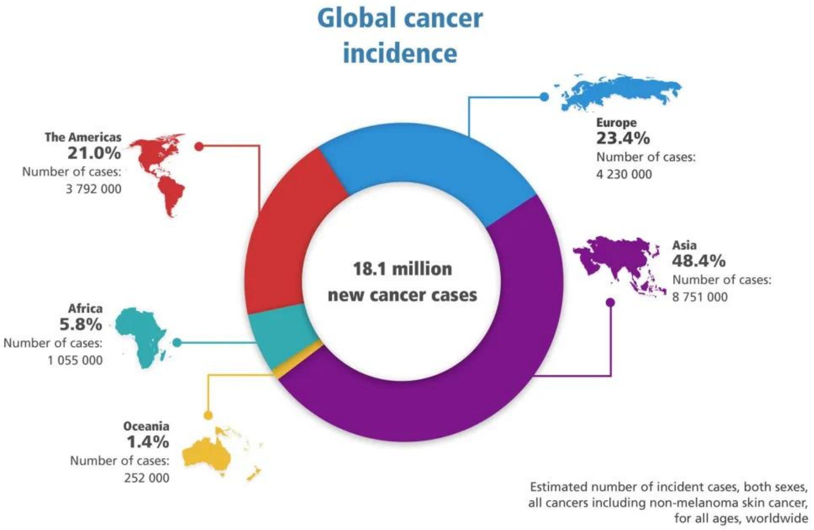

***Figure 1.1**- Estimated cancer cases worldwide.[30]*

Globally, the burden of cancer is a major public health concern. An estimated 10 million people die from cancer each year, making it an important threat to the public's health. There will be over 1,958,310 new cases of cancer in total in 2023, about 5370 cases every day.

Prostate, lung and bronchus, and colorectal cancers (CRC) are the most prevalent cancers diagnosed in 2023; prostate cancer alone accounts for 29% of men's cancer diagnoses. On the other hand, 52% of new diagnoses in women are for lung cancer, CRC, and breast cancer, with breast cancer alone accounting for 31% of all female cancers.

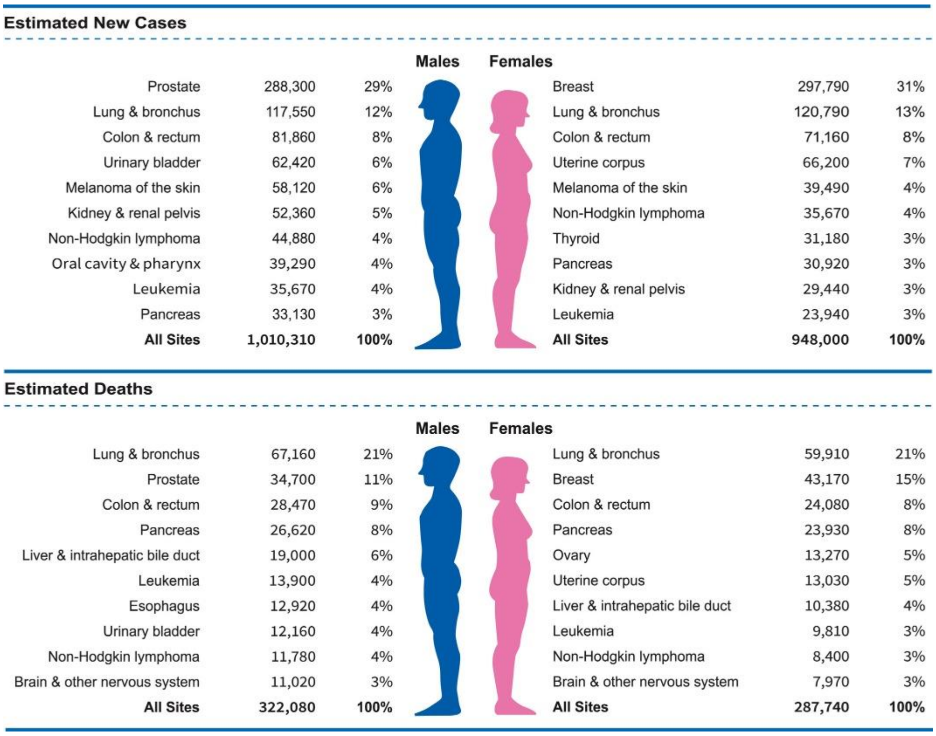

Estimated New Cases

Males			Females		
Prostate	288,300	29%	Breast	297,790	31%
Lung & bronchus	117,550	12%	Lung & bronchus	120,790	13%
Colon & rectum	81,860	8%	Colon & rectum	71,160	8%
Urinary bladder	62,420	6%	Uterine corpus	66,200	7%
Melanoma of the skin	58,120	6%	Melanoma of the skin	39,490	4%
Kidney & renal pelvis	52,360	5%	Non-Hodgkin lymphoma	35,670	4%
Non-Hodgkin lymphoma	44,880	4%	Thyroid	31,180	3%
Oral cavity & pharynx	39,290	4%	Pancreas	30,920	3%
Leukemia	35,670	4%	Kidney & renal pelvis	29,440	3%
Pancreas	33,130	3%	Leukemia	23,940	3%
All Sites	**1,010,310**	**100%**	**All Sites**	**948,000**	**100%**

Estimated Deaths

Males			Females		
Lung & bronchus	67,160	21%	Lung & bronchus	59,910	21%
Prostate	34,700	11%	Breast	43,170	15%
Colon & rectum	28,470	9%	Colon & rectum	24,080	8%
Pancreas	26,620	8%	Pancreas	23,930	8%
Liver & intrahepatic bile duct	19,000	6%	Ovary	13,270	5%
Leukemia	13,900	4%	Uterine corpus	13,030	5%
Esophagus	12,920	4%	Liver & intrahepatic bile duct	10,380	4%
Urinary bladder	12,160	4%	Leukemia	9,810	3%
Non-Hodgkin lymphoma	11,780	4%	Non-Hodgkin lymphoma	8,400	3%
Brain & other nervous system	11,020	3%	Brain & other nervous system	7,970	3%
All Sites	**322,080**	**100%**	**All Sites**	**287,740**	**100%**

Figure 1.2- *2023 estimated new cancers and deaths.[24]*

On the other side, survival rates have increased recently as a result of advancements in cancer detection, innovative therapeutics, and treatment methods. For instance, in the past 30 years, the survival rate for chronic leukaemia has risen from 22% to 70%.

Since 1991, there has been a steady decline in the cancer mortality rate, accounting for almost 3.8 million cancer deaths avoided.[2]

Nevertheless, a significant number of people are affected by tumours daily, which differ from one another in terms of type, location, and developmental stage. Many of these cancers have been effectively treated in recent years, and therapies are now widely accepted as safe and effective. There are numerous cancer treatment options available today, each using unique tactics, methods, and resources. Traditional therapies include hormone therapy and chemotherapy. photodynamic therapy (drugs activated by light), radiation therapy (therapy using boron, argon, or proton), stem cell, and targeted therapy are among the treatments that aid the immune system in fighting cancer. [21]

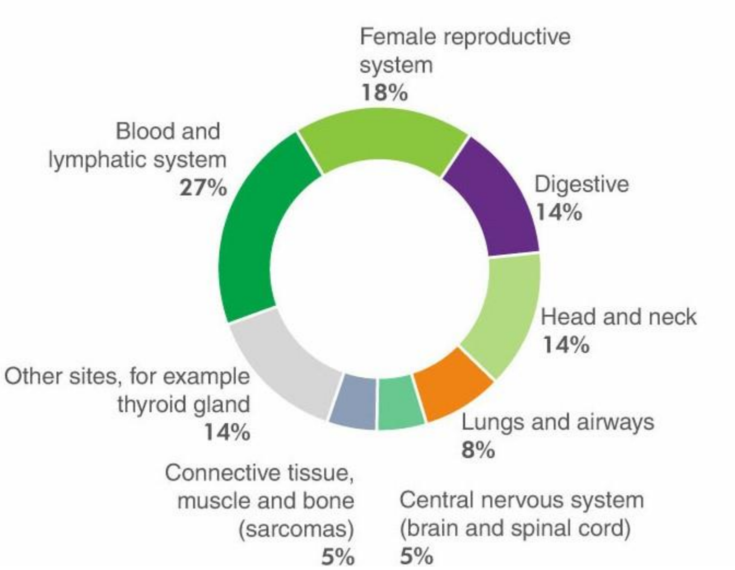

Figure 1.3- *Rare cancer locations inside the body.[14]*

On the other hand, there are malignant cancers that are yet poorly understood, whose therapies are not standardised yet. Most of them remain unreliable, excessively complex, and intrusive.

One of the fastest-growing cancer forms in the USA, for instance, is liver cancer, which is becoming more common despite being a rare disease. According to medical professionals, 1% of American men and women will get a liver cancer diagnosis at some point in their lives.[5]

Hence, a deep interest in the medical society has growth for minimally invasive treatments since they offer advantages over traditional surgery such as faster recovery times, reduced scarring, more efficiency, and fewer aftereffects on the patient.

The thesis work will be concentrated on hyperthermia therapy, which seeks to induce tissue heating to cause malignant cell necrosis. Hyperthermia to treat cancer is also called thermal therapy, thermal ablation, or thermotherapy.

Part I
Minimally invasive treatments

Chapter 2

Introduction

Cancer care has changed significantly as a result of minimally invasive cancer treatments, which give patients and medical professionals novel techniques to diagnose and treat cancer that are less intrusive and enhance patient outcomes. Laparoscopic surgery, robotic-assisted surgery, radiofrequency ablation, cryoablation, and several interventional radiology procedures are only a few examples of the many minimally invasive techniques available. A constant development of new methods and technology is always in process.

These therapies do, however, have drawbacks and restrictions. For instance, not all of them are suitable for all cancer forms or stages of the disease.[29]

2.1 Thermal ablation

Thermal ablation is a medical technique used to treat specific cancers. It entails the destruction or damage of malignant tissue using heat.

Thermal ablation can be done in a variety of ways, each having unique benefits and uses. Radiofrequency ablation (RFA), microwave ablation (MWA), laser ablation (LA), high-intensity focused ultrasound (HIFU), and cryoablation are the most often employed ones.

Advanced malignancies such as those of the appendix, bladder, brain, breast, cervical, esophageal, head and neck, liver, lung, melanoma, mesothelioma, sarcoma, and rectal have all been treated with hyperthermia.

2.1.1 Radiofrequency ablation (RFA)

RFA produces heat and kills cancer cells by using high-frequency electrical currents. The radiofrequency waves lead the cells to die when a specialised needle or probe is introduced into the tumour. RFA is frequently applied to tumours of the liver, kidney, lung, and bone.

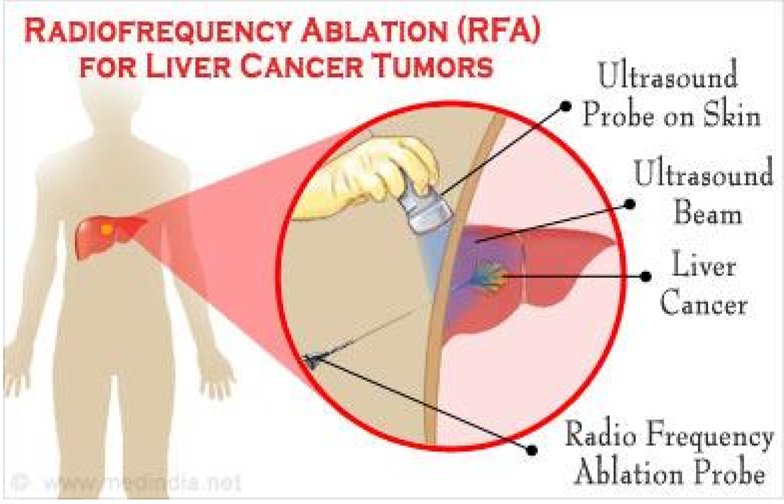

Figure 2.1- example of working principle of RFA.[20]

The electrical conductivity of tissue has a significant role in heat production. Because malignant tissue has a higher electrical conductance than normal tissue, the majority of electrical current flows through it, causing heat to build up in the affected area. Additionally, compared to normal tissue, malignant tissue has a higher heat conductivity, which aids in keeping heat in this region and protecting nearby normal parenchyma.

However, RFA is subject to several constraints. Firstly, a variety of RFA devices function in a monopolar mode and have grounding pads that are affixed to the skin, potentially causing skin burns. Secondly, potential charring of the tissue surrounding the electrode during ablation affects both electrical and heat conductance. The "heat sink" phenomenon is an additional issue: heat can be drained from the ablation zone by large blood arteries and airways, which lowers the temperature to a sublethal threshold and reduces the efficacy of ablation. Hence, when treating lesions next to big veins or airways, it is advised to switch to MWA or cryoablation, which is less susceptible to heat sink.[20]

2.1.2 Microwave Ablation (MWA)

MWA uses microwave energy to burn up and destroy specific tissue. Tumours of the liver, lungs, and kidneys are frequently treated with it.

The application of an electromagnetic field, usually between 900 and 2500 MHz, can heat tissues to fatal temperatures, resulting in tissue damage.

The fluctuating electric field forces polar molecules (mostly water) in tissue to constantly realign, which raises the kinetic energy and, consequently, the tissue's temperature. For this kind of heating, tissues with a high-water content work well. An interstitial antenna, which couples’ energy from the generator power source to tissue, allows microwave energy to radiate into the tissue.

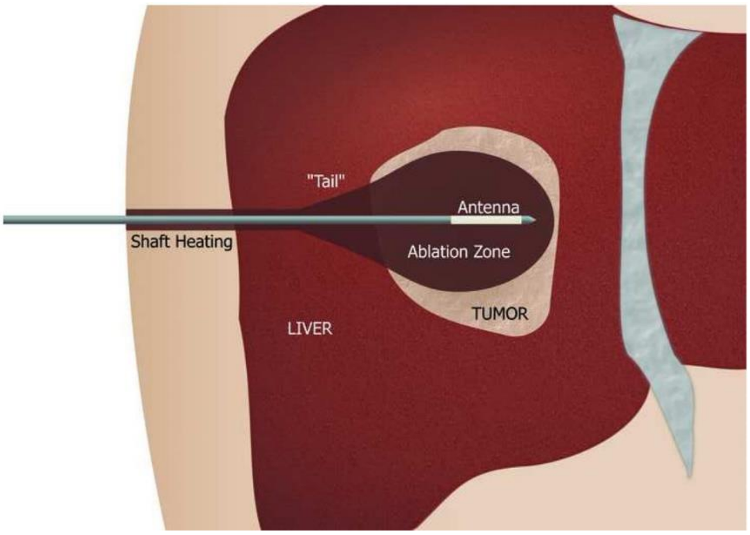

***Figure 2.2**- MWA treatment.[16]*

Unlike RFA and LA, the carbonised or desiccated tissues, that tend to accumulate around all hyperthermic ablation applicators, can be here easily penetrated by microwaves.

Another tissue feature that can affect how efficiently energy propagates through tissue is relative permittivity, which is a measure of how well a substance or tissue absorbs an electric field.

When situated close together, multiple microwave antennas can be energised concurrently to benefit from thermal synergy, or they can be widely spaced apart to simultaneously ablate multiple tumours.

The capacity to phase and position antennas to take advantage of electromagnetic field overlap is another feature that sets microwave ablation apart from the other thermal therapies. When phased constructively, higher temperatures and more efficient heating is achieved.[16]

2.1.3 Laser surgery

Laser ablation uses powerful, precisely focused laser beams to treat a range of illnesses, including cancer.

By using thermal ablation, laser surgery aims to eradicate tumours of the skin, lungs, vulva, cervix, penis, and vagina.

Although laser burning sounds quite harmful, due to its less invasiveness than conventional surgery, less cutting and damage are involved. For example, the laser can be aimed without making a major cut opening, using fibre optics and specialised scopes. The tumour is then carefully targeted for destruction with the laser.

LA, characterized by the laser, the power source, a lasing medium, and reflecting mirrors, produce monochromatic light, the wavelength of which determines the laser's characteristics and how it interacts with biological tissue. The material used to transfer laser light into deep organs is often a flexible optical fibre with a small diameter.

Three processes can be used to explain the interaction between a laser and tissue: scattering, reflection, and absorption.

Some aspects need to be considered throughout the treatment in order to eradicate the tumour without harming the healthy surrounding like the absorption length, which is the tissue depth required to absorb the input light.

The absorption length varies depending on the type of laser used and is also influenced by the optical properties of the tumour and the adjacent healthy tissue.

LA can be carried out either continuously or intermittently. Low laser power (2 W or 3 W up to 30 W) and long treatment times are typically used in continuous mode. Higher laser power (larger than 100 W) is employed in the pulsed mode, where the laser energy is emitted in a sequence of pulses.[8]

2.1.4 Cryosurgery

Cryosurgery uses extreme colds to treat a wide range of medical ailments. This method, which is sometimes referred to as cryotherapy or cryoablation, provides a novel way to destroy tissue by freezing it and then removing any undesirable or aberrant tissue.

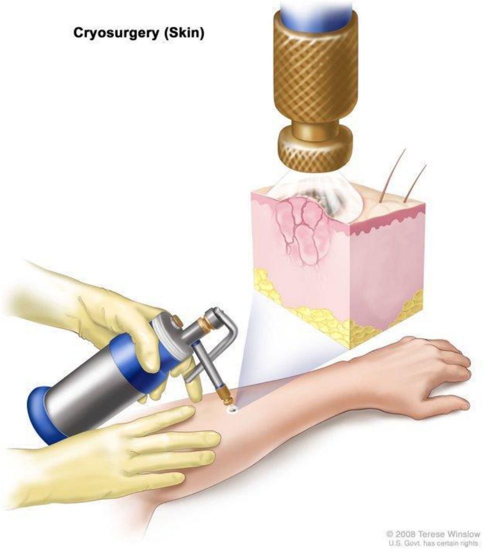

***Figure 2.3**- Cryosurgery application.[32]*

In cryosurgery, aberrant cells are frozen and killed using a liquid nitrogen spray or an extremely cold probe. Sometimes precancerous problems affecting the skin, cervix, and penis are treated with this approach. Certain tumours, such as those of the liver and prostate, can also be treated with cryosurgery. The location of the cancer cells may be determined by using a scan (ultrasound or CT scan) to direct the probe. This minimises harm to neighbouring healthy tissue.

However, the progress of cryosurgery therapy is still slow. Due to its great complexity, the field of cryoinjury has not largely progressed yet.[32]

2.1.5 High intensity focused ultrasound (HIFU)

HIFU uses ultrasonic waves, that are extremely precise, on a particular target inside the body. At the focal point, these waves produce heat that can be used to damage or ablate tissue via coagulation. The secret to HIFU's effectiveness is its capacity to provide therapeutic effects without requiring invasive surgical techniques or incisions.

High-intensity focused ultrasound and imaging techniques that give three-dimensional anatomy for accurate tumour targeting are used to cause the tumour to ablate.

Treating prostate cancer in patients who might not be good candidates for radiation therapy or conventional surgery, is one of the most prominent uses of HIFU.[34]

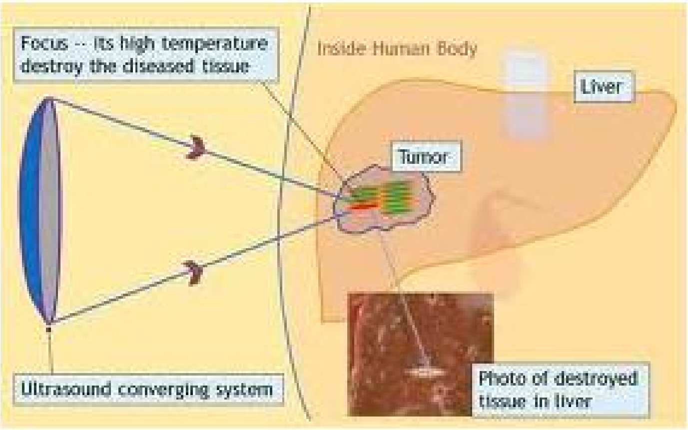

Figure 2.4- *HIFU working principles.[34]*

2.2 Electrosurgery

This technique employs electrical energy to cut, coagulate, or remove tissue, providing accuracy, effectiveness, and little blood loss.

High-frequency electrical currents are used in electrosurgery to provide targeted heat at the operative site. Depending on the surgical goals, this heat can be used for cutting, coagulation to stop bleeding during surgery, or tissue removal.

Electrosurgery is now essential for blood loss minimization which lead to shorter operating time, improving patient results.

2.3 Mohs surgery

Mohs surgery is becoming a key therapy method for skin cancer. This surgical technique is unique in its accuracy and efficacy, which aid in the elimination of cancer while protecting healthy tissue.

A comprehensive and accurate approach is made possible by the combination of real-time microscopic examination and surgery. Certain skin cancers are removed by doctors by shaving off a very tiny layer at a time. This process is iterated until every cell in a layer exhibits normalcy.

Among skin cancer therapy procedures, it offers one of the greatest cure rates due to its high level of precision. Moreover, the procedure is quite successful in minimising scarring and accelerating healing.

Mohs surgery is utilised to preserve as much healthy tissue as possible, especially when the extent of the cancer is unknown,

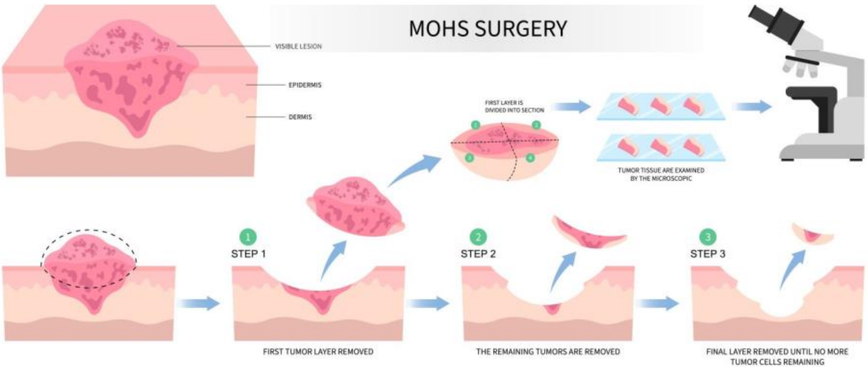

Figure 2.5- *Mohs surgery stages.[4]*

2.4 Laparoscopic surgery

A laparoscope is a thin, flexible, long tube that is used to examine into the body through a small cut. Biologic procedures like tissue samples removing for cancer occasionally employ it. Research has shown that certain tumours can be removed using the laparoscope by creating tiny punctures and utilising long, thin devices. This can lessen pain following surgery and blood loss during the procedure. Additionally, it expedites recovery and reduces hospital stays.

For certain tumours of the colon, rectum, liver, prostate, uterus, and kidney, doctors can perform laparoscopic procedures in a safe and efficient manner.

2.5 Thoracoscopic surgery

Once the lung collapses, a small incision can be made in the chest to insert a thin tube called a thoracoscope, which has a tiny video camera attached to its end. Thanks to this, doctors are able to remove tiny tumours from the lung's surface, drain fluid from any troublesome regions on the lining of the chest wall, and get tissue samples.

Less cutting is required during this kind of surgery, which has even been used to remove cancerous lung sections. According to studies, the outcomes of this method for treating early-stage lung cancer are comparable to those of removing a portion of the lung by a cut in the side of the chest.

2.6 Robotic surgery

In robotic surgery, surgical tools are controlled by the physician using accurate robotic arms. These are mainly employed during laparoscopic or thoracoscopic procedures. The benefits of this kind of surgery are similar to those of laparoscopic and thoracoscopic surgery. They can indeed lessen pain following the procedure and blood loss during it, minimising hospital stays and hastening the healing process.

2.7 Stereotactic radiation therapy

With very little effect on the surrounding healthy tissue, stereotactic radiation therapy delivers a high dose to a small tumour area by utilising radiation sources from various angles.

This procedure is mostly used to treat brain tumours, although it can also be used for neck, lung, spine, and other tumour sites.

During stereotactic radiosurgery, physicians employ three different technologies to deliver radiation to the brain and other parts of the body:

Linear accelerators (LINACs), which are X-ray-using devices; Gamma Knife machines, employing about 200 small gamma-ray beams; and proton beam therapy, which takes advantage of charged particles. [15]

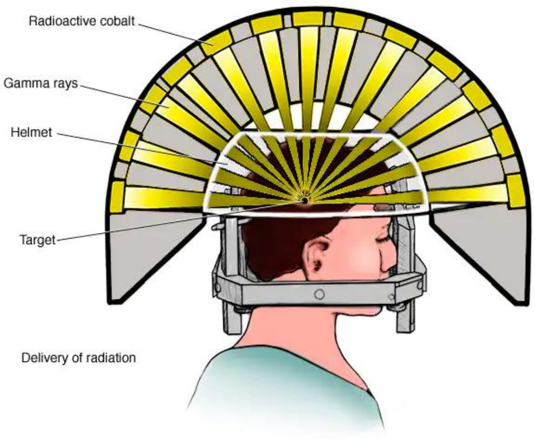

© MAYO FOUNDATION FOR MEDICAL EDUCATION AND RESEARCH. ALL RIGHTS RESERVED.

***Figure 2.6**- Stereotactic therapy delivery system.[15]*

Part II
Lasers

Chapter 3

Laser, Optical Fiber, Fiber Bragg Gratings

3.1 Introduction

The objective of the thesis is to provide medical crews with a device able to monitor thermal processes for laser thermotherapies and support them for the treatment planning.

The heat source absorbed by the biological tissue consists of a laser radiation delivered by an optical fiber. The monitoring system exploited for the experimental session instead is made of Fiber Bragg Gratings array. To better understand the work done, a brief introduction of their working principle and applications is here described.

3.2 Laser

The word Laser stands for Light Amplification by Stimulated Emission of Radiation. The term, which refers to both a physical principle and a technological device, can be applied to a variety of industrial processes. Since they were first proposed in the early 20th century, many industries have seen revolutionary change as a result of their development and application. Lasers have made revolutionary strides and changed the way we live in a variety of fields, including communication, healthcare, industry, and even entertainment.

The radiation stimulated emission theory, which today serves as the foundation for laser operation, was first drafted by Albert Einstein in 1917.

However, Theodore H. Maiman created the first functional laser on May 16, 1960 at Hughes Research Laboratories in Malibù, California.

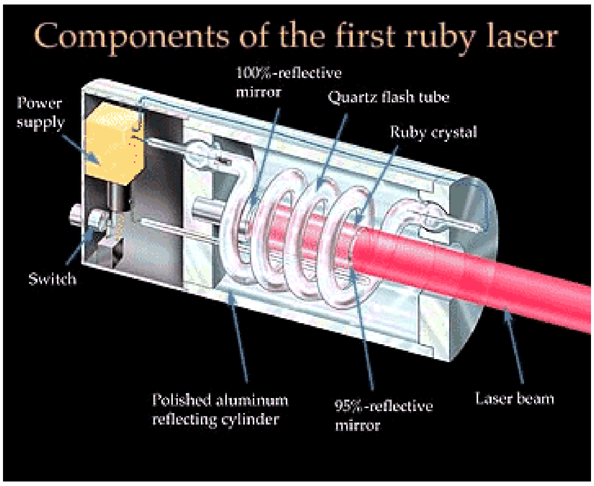

Figure 3.1- *Ruby's laser.[13]*

Lasers are machinery that use the stimulated emission process to create focused, coherent beams of light. They are made up of three essential parts: an optical resonator, an energy source, and an active medium. The atoms or molecules in the active medium, such as a crystal, gas, or semiconductor, have the ability to emit and amplify light. The atoms or molecules are stimulated by the energy source, or “pump”, which is commonly an electrical current or light, to produce photons. After being constrained inside the optical resonator, which is typically made up of mirrors or lenses, the photons begin to bounce off of one another, producing a precise and powerful beam of light. Lasers are usually named according to the type of lasing medium exploited.

We must explore the atomic level to comprehend the fundamentals of how lasers operate. Atoms can leap from low-energy orbitals (the ground state) to high-energy orbitals when the right amount of energy is given to the atom, which causes energy absorption and atomic excitation.

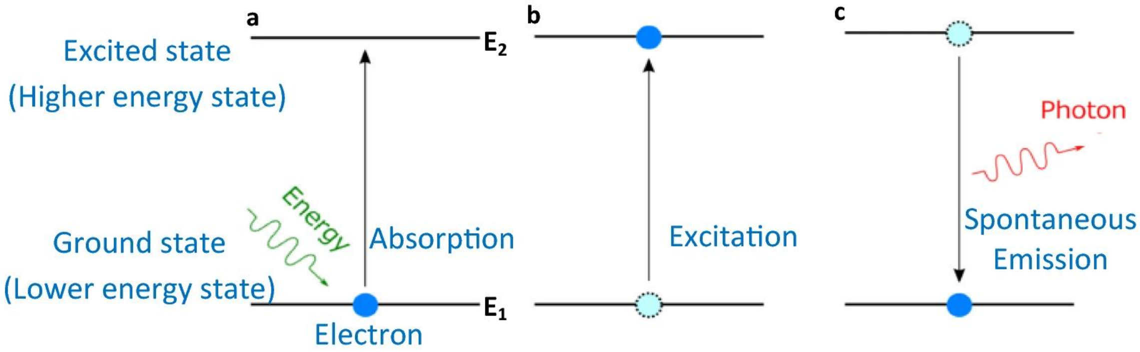

Figure 3.2- Absorption, excitation, spontaneous emission.[1]

As can be seen in Figure 3.2, electrons in the high-energy orbit spontaneously return to the ground state, the most stable one. The energy difference is released as a photon, whose frequency depends precisely on the energy difference between the two states and has an arbitrary phase and direction. This process is known as spontaneous emission.

This photon's emission may strike one of the mirrors in the resonating cavity and bounce back into the lasing medium, where it may strike other excited atoms. A collision with an excited atom can lead to its return to its ground state, producing two photons that are identical in direction, phase, polarization, and energy (frequency). The term of this procedure is stimulated emission.

Numerous atoms quickly begin to emit light along the same axis as a result of the cascade effect of stimulated emission of photons, which causes further amplification (optical gain). The term "population inversion" refers to the requirement for the majority of the atoms to be kept in the excited state in order for a laser to continue functioning. This is accomplished by either a continuous energy pump input (continuous wave laser) or an intermittent energy pump input (pulsed wave laser).

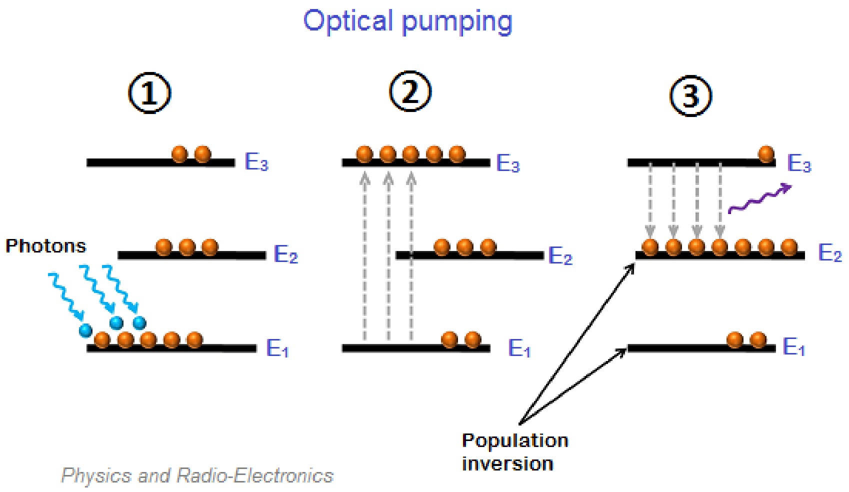

*Figure **3.3**- Population inversion diagram.[23]*

Once created, photons are permitted to leave the lasing medium through the partially reflecting mirror. This laser light can be in the visible spectrum or in the infrared or ultraviolet range. It is directed to the target via a delivery system that uses a series of mirrors for infrared or fiber-optic light guides for visible light.

The adaptability and accuracy of lasers have been fully acknowledged by the scientific community. Lasers, for instance, make it possible to analyse light-matter interactions in great detail in the discipline of spectroscopy. Additionally, laser-based methods like confocal microscopy and fluorescence spectroscopy have opened opportunities for the study of biological processes at the cellular level and medical imaging.

Lasers have transformed surgical techniques in medicine by giving surgeons unmatched precision and reducing patient trauma. Improved visual outcomes and quicker recovery times are now possible with eye procedures like LASIK and cataract removal thanks to laser-assisted methods. Additionally, lasers are used in dermatology, dentistry, and oncology to perform non-invasive treatments, destroy tissue, and deliver focused therapy for a variety of diseases.

In the industrial and technological fields, lasers have had a tremendous impact. Laser welding and cutting are now standard procedures in the manufacturing industry, providing accurate and effective substitutes for older technologies. Their capacity to precisely focus energy enables complex and quick material processing, which boosts output and improves quality.

Lasers also play a significant role in the transmission of data over great distances via fiber-optic networks in the telecommunications sector. Information can be sent at fast rates with little loss by encoding it into light pulses and using laser-based amplifiers and detectors. This technology has enabled worldwide communication, helped the internet expand, and changed how we interact and access information.

Additionally, lasers are now widely used in daily life. Lasers are widely used in consumer electronics, from barcode scanners and laser printers to DVD players and optical storage media. Security systems, laser pointers, and even the burgeoning field of lidar technology used for accurate mapping and navigation in driverless vehicles have all found uses for them.[26]

3.3 Diode laser

Gas lasers, dye lasers, solid-state lasers, fiber lasers, and diode lasers are the five basic categories into which lasers are divided.

The laser diode will be the type of laser used in the experimental component; thus, we will concentrate on it in this section.

Compact, solid-state diode lasers use semiconductors to produce coherent light, and they are made of a solid-state design. They are built with components like gallium arsenide (GaAs) or gallium nitride (GaN). They operate by passing electrical current through the semiconductor material, which enables coherent photon emission. Diode lasers are portable application-friendly due to their small size. They can emit light in a variety of wavelengths, from ultraviolet (UV) to near- and mid-infrared (NIR and MIR). They can function as pulsed emitters or continuous waves (CW) emitters.

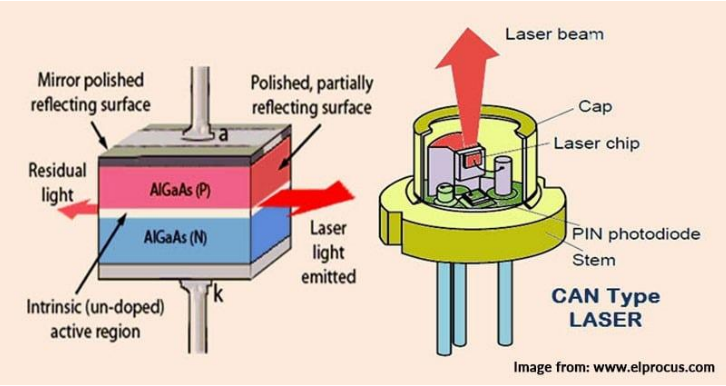

__Figure 3.4__- Diode laser components and functioning mechanism.[7]

By promoting photon emission at a semiconductor junction, diode lasers generate light. A p-n junction is the main component of a diode. Positively charged carriers (holes) are produced in excess in the p-type region compared to negatively charged carriers (electrons) in excess in the n-type region. A depletion area is created between the two materials by the connection. Current flows across the junction when a forward bias voltage (+ V_e to the p material and - V_e to the n material) is applied. Charge carriers move across the junction as a result. The depletion area receives injections of holes and electrons from the p and n regions, respectively. A photon is released for each charge that is cancelled when the two collide and neutralize.

The ends of the diode laser are made with reflective surfaces that create an "optical cavity." Internal reflection of the photons is enhanced by optical feedback, which produces narrow-band, coherent light. Another type of stimulating emission is when an excited electron is stimulated by a photon, resulting in the emission of another photon. Since these extra photons and the triggering photon are similar, amplification results. The laser energy becomes more intense while the stimulated emission continues, and photons are reflected inside the cavity.[28]

3.4 Optical fiber

An optical fiber is a flexible glass or plastic fiber that can transfer light and allow transmission over great distances. Due to their low losses and immunity to electromagnetic interference, which metal wires are susceptible to, fibers are mostly employed nowadays.

The light sent in an optical fiber is captured and contained within the fiber core using the optical technique known as "total internal reflection" (TIR). An optical fiber has a core that transmits light in the center and is encased in a cladding that traps light in the core. Glass fiber is than protected from the environment and made easy to handle for splicing or termination by a plastic buffer covering.

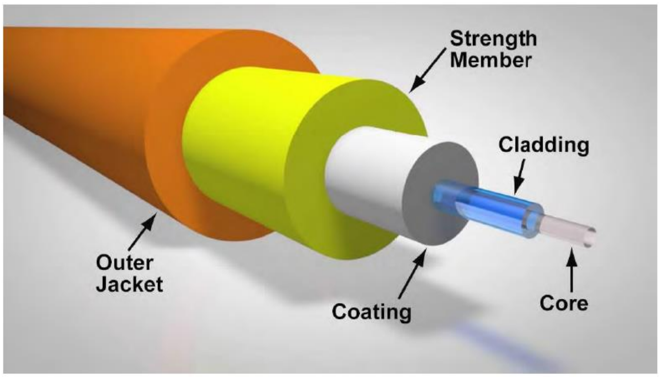

Figure 3.5- Optical fiber structure.[10]

Light bends due to differences in the index of refraction, which is a property of optical materials used to measure the speed of light in glass or any other optical substance. If the angle is surpassed, refraction will cause the surface to reflect light. All the light will be contained in the fiber core thanks to the correct index of refraction of the materials used for the core and cladding. "Total internal reflection" occurs if the angle of the light is below a predefined one. Optical fibers exploit this concept, described in Figure 3.6.

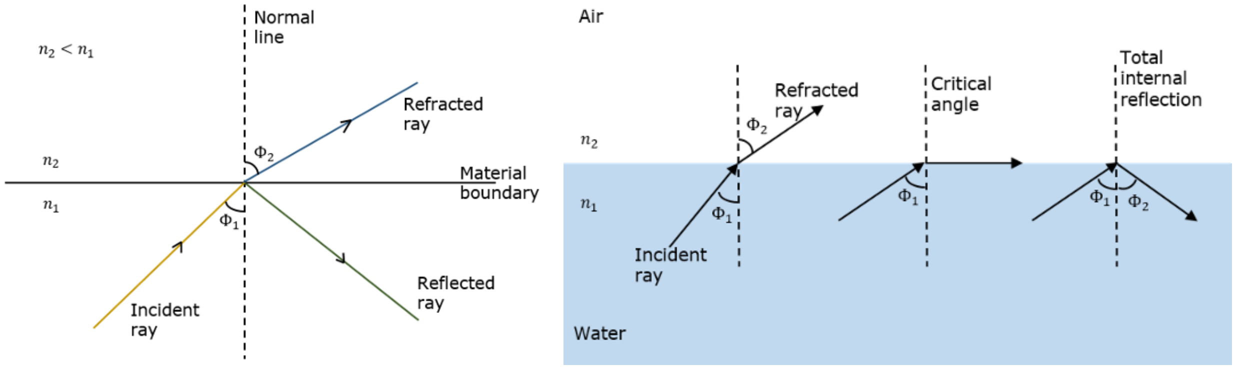

__Figure 3.6__-light behaviour in domains.[18]

In fact, reflected and refracted beams are produced for every incident beam of radiation. High angles will cause light to be refracted and lost within the fiber's cladding. As a result, there will be a radiation loss for every interaction with a material. Snell's law can be used to determine the angle that specifies TIR, preventing any information transmission loss. The "numerical aperture" (NA) of the fiber, a common fiber specification, is determined by the total internal reflection angle.

An optical fibre can propagate one or more electromagnetic field configurations depending on the fibre core size, operating wavelength, and core-cladding refractive index difference.

There are mainly two types of optical fiber: Single mode and multimode.

Single mode fibres typically have a core diameter of 9 micrometers and beam intensity profiles with a Gaussian distribution.

Since the glass fiber core of single-mode fiber has a lower diameter, it can be used across greater distances. The likelihood of attenuation, or a weakening of the signal,

is reduced by the smaller diameter. The narrower opening concentrates the light into a single beam, providing a more direct path and extending the signal's range.
Additionally, single-mode fiber has a far wider bandwidth than multimode fiber. Typically, a laser is utilized as light source for single-mode fiber. Because it takes precise calculations to create the laser light in a smaller hole, single-mode fiber is typically more expensive.
Step index multimode fiber was the first fiber design. They have a much greater core diameter, ranging from 50 to over 400 micrometers, which is made completely of one type of optical material whereas the cladding of another type with different optical characteristics. Because of the bigger core aperture, multimode fiber is used for shorter distances so that light signals can bounce and reflect more. More data can be transmitted because more light pulses can be sent via the cable at once due to its wider diameter. However, this also means that there is a greater chance of signal loss, decrease, or interference. In multimode fiber optics, the light pulse is typically produced by a LED.

Fluorescence sensors, interferometric sensors, distributed temperature sensors, emissivity-based sensors, and fiber Bragg gratings are the basic categories of temperature sensors. The thesis focuses on FBGs since they offer the best mix of technological maturity and sensing performance, making them the most promising technology for heat treatment monitoring. [10]

3.5 Fiber Bragg Gratings Sensors

A fiber Bragg grating (FBG) is a type of distributed Bragg reflector that is built into a brief section of optical fiber and reflects some wavelengths of light while transmitting all others. This is accomplished by periodically changing the fiber core's refractive index, which results in the creation of a dielectric mirror that is tuned to a certain wavelength.

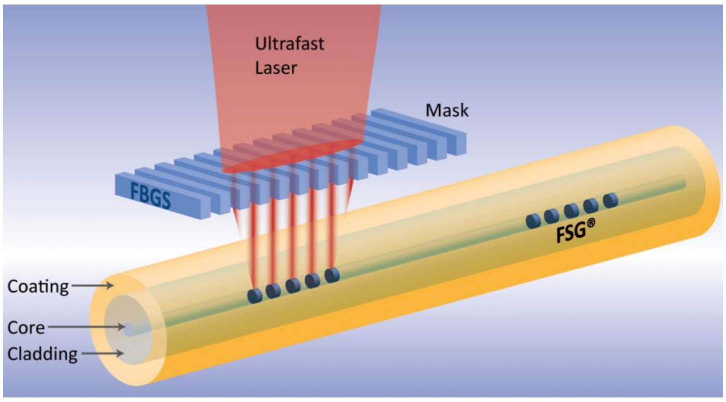

Figure 3.7*- FGB working principle.[9]*

Fiber Bragg Gratings are created by exposing a single-mode fiber's core laterally to a periodic pattern of intense laser light. The exposure causes the fiber's core's refractive index to permanently rise, resulting in a fixed index modulation that follows the exposure pattern. The term "grating" refers to this fixed index modulation.

A small amount of light is reflected with each periodic shift in refraction. When the grating time is roughly half the wavelength of the input light, all the reflected light signals combine coherently to one vast reflection at a specific wavelength. The wavelength at which this reflection takes place is known as the Bragg wavelength, and this circumstance is known as the Bragg condition. Light signals that are not phase matched and have wavelengths other than the Bragg wavelength are transparent.

Therefore, there is little signal fluctuation or attenuation as light passes through the grating. Only the Bragg-conforming wavelengths are impacted and powerfully back-reflected. One essential characteristic and benefit of fiber Bragg gratings is their ability to precisely setup and maintain the grating wavelength.

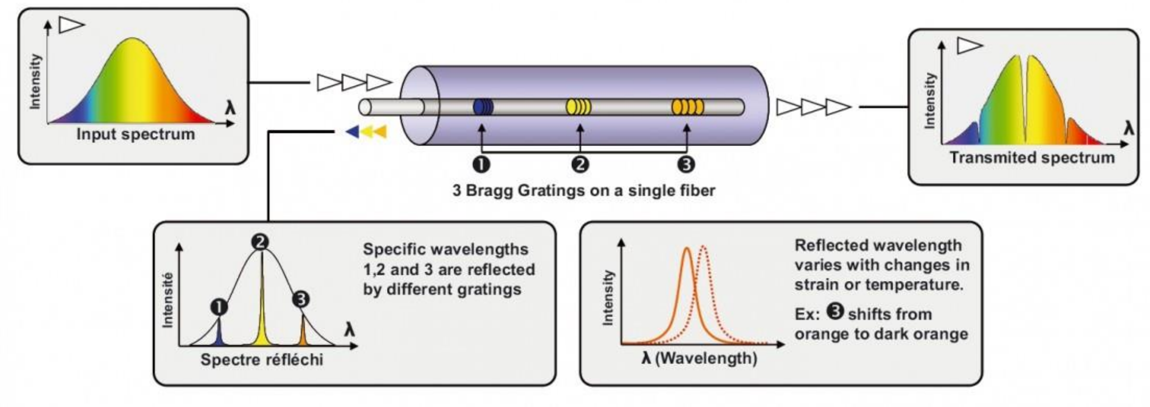

Figure 3.8- *FBG sensor operating principles.[9]*

The reflected component's centre wavelength fulfils the Bragg relation, which states:

$$\lambda_{Bragg} = 2n\Lambda \qquad (1)$$

n is the index of refraction and Λ is the frequency of the FBG's index of refraction fluctuation. The wavelength of the reflected component will fluctuate as a function of temperature and/or strain because the parameters n and Λ are temperature and strain dependent. This well-known relationship makes it possible to infer the temperature or strain from the refracted FBG wavelength.[25]

Part III

Simulation Activities

Chapter 4

Bio-heat transfer equation

4.1 Laser-tissue interaction

Once a laser beam has been created, it is directed at tissue to carry out a particular function. There will be one of four interactions once the energy enters the biological contact.

- Absorption: The photons are absorbed by particular molecules in the tissue known as chromophores, which are molecules in a given material that absorb particular visible light wavelengths and give the material colour. The work is then done by converting the light energy into other heat. Absorption is the most significant interaction.
- Reflection: Without any penetration or interaction, the laser beam simply bounces off the surface. Reflection is typically an undesirable side effect; however odontology processes provide a helpful example of reflection.
- Transmission: The laser energy can interact with deeper tissues by penetrating superficial tissues. For example, during retinal surgery, the laser treats the retina by piercing the lens. Tissue transmission is further demonstrated by the NdYAG and diode lasers' deeper penetration.
- Scattering: The laser energy will disperse in different directions once it has reached the target tissue. When exposed to certain bio stimulative wavelengths, this phenomenon can be beneficial.

There are five important types of biological effects that can occur once the laser photons enter the tissue: fluorescence, photothermal, photo-disruptive, photochemical, and photo-biomodulation.

When tissue molecules are exposed to laser light, fluorescence occurs. This results in the emission of light at a second wavelength.

The effects of photothermal radiation are examined in this thesis paper. They happen when heat is produced as a result of the chromophores absorbing the laser energy. To incise or remove tissues, this heat immediately vaporizes the tissue. These operations generate heat, hence extreme caution must be used to prevent thermal harm to the tissues.

Understanding photo-disruptive effects (also known as photoacoustic) can be a little more challenging. Photo-disruptive ablation is a procedure used to eliminate hard tissues. Rapid thermal expansion of the water molecules in the tissue is caused by interaction between short-pulsed bursts of laser light with exceptionally high power and the tissue's water content. This results in a thermo-mechanical acoustic shock wave that can effectively disrupt bone matrices. When used appropriately, no residual heat is produced, which is especially true when the idea of thermal relaxation is taken into account, making thermal damage extremely improbable. Dental care is the principal use of this procedure.

Instead, photon energy triggers chemical reactions, which are known as photochemical reactions.

Lasers' capacity to hasten healing, boost circulation, lessen edema (lymphatic fluid-induced tissue swelling), and lessen discomfort is known as photo-biomodulation.

These effects are influenced by the laser's peak power, wavelength, and the temperature characteristics of biological tissues.

Dr. Kelly wrote the first study on laser coagulation, which was published in 1967. He used a laser to treat pre-retinal haemorrhage in rabbits and stressed that a higher intensity setting could result in the destruction of the retina's nerve fiber. Lasers have the ability to raise cellular temperature and cause denaturation of collagen and proteins, which causes tissue to clot and can necrotize cells.

A rise in body temperature has a number of negative impacts on the body, including hyperthermia, coagulation, and other permanent tissue damage. Hyperthermia is the immediate result of raising the temperature. The hyperthermia domain, which is often between 40 and 50 degrees Celsius, is where some molecular connections are broken, and the membrane is changed. It is noted that enzyme activity has decreased. In this temperature range, the effects are reversible.

Proteins and collagen become denaturised at temperatures about 60°C, which can necrotize cells and cause tissue to coagulate. Numerous optical procedures, including LITT and hair removal, target temperatures greater than 60°C. As the permeability of cell membranes rises with temperature, the balance of chemical concentration is broken.

Water starts to evaporate at a temperature of 100°C. Because gas bubbles are generated during the vaporization phase and the temperature of the tissue does not change, the process is occasionally referred to as the thermomechanical one. Fragments of tissue decompose thermally as result of the growth of these bubbles and changes in their volume. If all water molecules evaporate, carbon atoms are liberated, resulting in the blackening of the nearby tissues and the production of smoke from the skin. Carbonization is the term for this stage. Finally, melting could start to happen above 300°C. The effects of heat at various temperatures are listed in Table 1.[18]

Temperature	**Biological effects**
37°C	Normal
45-50°C	Hyperthermia, Reduction of enzyme activity, Cell immobility
60-80°C	Denaturation of proteins and collagen; Coagulation
100°C	Vaporization, Thermal decomposition (ablation)
>100°C	Carbonization
>300°	Melting

Table 1*- Temperature effects on biological tissues.[19]*

4.2 Bioheat equation

A temperature differential causes a phenomenon known as heat transfer to happen between domains or between distinct areas of the same object. Convection, radiation, and conduction can all transfer heat depending on the condition of the material involved in the occurrence.

Instead, the term "bioheat transfer" describes the transport of heat within biological tissues. It is comparable to conventional heat transfer in solids, and all the thermal mechanisms mentioned above are applicable. It is also necessary to account the heat transport processes unique to biological tissues. The first of these tissue-specific mechanisms is metabolic heat, produced as a result of cell metabolism. The second factor that must be taken into account is blood circulation within the tissue, which frequently plays a major role in influencing tissue temperature during electromagnetic-energy-based thermal therapies.

The temperature of the tissue around a vessel differs from the temperature of the blood passing through the vessel lumen when thermal therapies such as thermal ablation or therapeutic hyperthermia are used. Convective heat transfer occurs as a result of this temperature differential between the blood and tissue. Blood flow-mediated cooling significantly affects tissue temperature in the majority of heat-based thermal therapies; hence it must be properly considered in any mathematical models that represent tissue temperature used for thermal therapies.

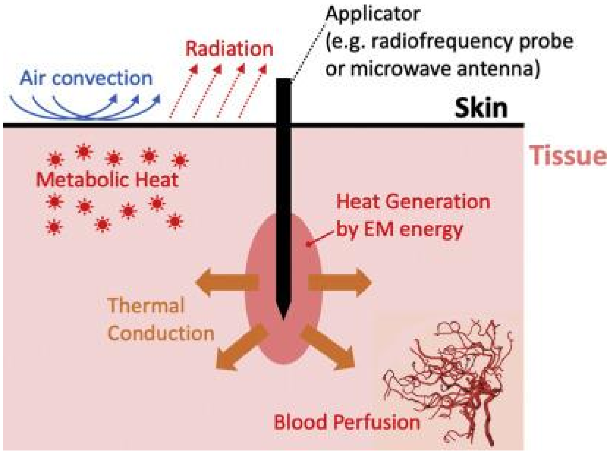

Figure 4.1- Bio-heat transfer processes' mechanism.[11]

Penne's bioheat transfer equation (PBHTE) is widely recognized as the standard model for predicting the temperature distribution within biological tissues. It covers a special descriptive term for the heat exchange which occurs between tissues and blood flow. It can be seen in Equation 2 shown below.

$$\rho c_p \frac{\partial T}{\partial t} + w_b c_b \rho_b (T - T_b) - \nabla(k \nabla T) = q_m + J \cdot E + Q_{laser} \tag{2}$$

Where q_m is the energy generated from the metabolism process [W/m^3], which can be usually neglected due to its small value; Q_{laser} is the source energy, in our case coming from the laser; J is the current density [A/m^2], E is the electric field [V/m]; w_b is the blood perfusion rate [1/s]; c_b is the blood specific heat [J/kg K]; ρ_b is the density of blood [kg/m^3]; T is the time-dependent temperature [°C]; T_b is the baseline temperature of arterial blood, that is constant with a standard value 37°C; c_p is the specific heat of tissue [J/kgK] and k is the thermal conductivity of tissue [W/m K], which can assume constant values.

For sake of simplicity, we analysed a simplified model, considered as the ideal one. The tissue was indeed considered isotropic and homogeneous. Nor vascular, arterial, venular roads, nor blood temperature differences were accounted.

In our model, metabolic heat and blood profusion were not examined.

Finally, we ended up with the classical Fourier's law for homogeneous media.

$$\rho c \frac{\partial T}{\partial t} = k \nabla^2 T + Q \tag{3}$$

Which, in case of no time dependence, reduces to:

$$k \nabla^2 T + Q = 0 \tag{4}$$

Instead, in case no external source is present, the equation can be expressed as follows.

$$\frac{\partial T}{\partial t} = \alpha \cdot \nabla^2 T, \qquad \alpha = \frac{k}{\rho c} \tag{5}$$

Where α is known as thermal diffusivity [m^2/s].

PBHTE, which is straightforward and has the best capacity to forecast the temperature parameter in various applications, has been employed as a hyperthermia model in several applications. Its significant disadvantages include the directionality of blood flow and the lack of a heat transfer mechanism.[3]

4.3 Green function

Generally speaking, a Green's function is an integral kernel that can be used to solve differential equations from a large number of families including simpler examples such as ordinary differential equations with initial or boundary value conditions, as well as more difficult examples such as inhomogeneous partial differential equations (PDE) with boundary conditions. Important for a number of reasons, Green's functions allow for visual interpretations of the actions associated to a source of force or to a charge concentrated at a point, thus making them particularly useful in areas of applied mathematics. In particular, Green's function methods are widely used in, e.g., physics, and engineering.[33]

We will exploit Green’s function to solve differential equations, like heat one, that present themselves as follow:

$$Ly(t) = f(t) \tag{6}$$

Where L is the linear differential operator and $f(t)$ a general time dependent function. Here we will focus on the solution of a particular problem, considering as function an impulse, i.e instantaneous source. The term “instantaneous” indicates that the source releases all its heat spontaneously at a time $\tilde{t}$ in a point r′ within the domain. Green’s function thus solves:

$$LG(t-\tilde{t}) = \delta(t-\tilde{t}) \tag{7}$$

Where $\delta(t-\tilde{t})$ expresses the Dirac delta force, equal to zero at every time except for time $t=\tilde{t}$. To exploit Dirac definition, we consider the right part of the equation as a superposition of pulses. Hence, integrating over the time domain, the equation reduces to the form:

$$L\int G(t-\tilde{t})f(\tilde{t})\,d\tilde{t} = \int \delta(t-\tilde{t})f(\tilde{t})\,d\tilde{t} = f(t) \tag{8}$$

For Equation 6, This implies that:

$$y(t) = \int G(t-\tilde{t})f(\tilde{t})\,d\tilde{t} \tag{9}$$

Equation 9 shows how the Green’s function represents the propagation in time response to an impulsive source $f(\tilde{t})$ applied at $\tilde{t}$.

Now, let’s consider a general time dependent heat equation:

$$\rho c_p \frac{\partial T}{\partial t} - \nabla(k\nabla T) = Q \tag{10}$$

Mandatory is the definition of a volumetric source, here chosen as an impulsive one and dependent on time:

$$q(\tilde{x}, t) = \delta(t)\delta^3(\tilde{x}) \tag{11}$$

The L differential operator is expressed by:

$$L = \frac{\partial}{\partial t} - \alpha \nabla_{3D}^2 \tag{12}$$

If the extension of the domain is infinite, the Green's function is called the fundamental solution of the following PDE:

$$\frac{\partial G}{\partial t} = k\nabla^2 G + \delta(t)\delta^3(\bar{x}) \tag{13}$$

Where $G(r, t)$ expresses the temperature at each domain point as a response to an impulsive source:

$$G(r, t) = \frac{1}{(4\pi kt)^{3/2}} exp\left(-\frac{r^2}{4kt}\right) \tag{14}$$

In this master’s thesis work we decided to apply the heat source for a specific time range able to assess both heating and cooling transients. Thus, for sources defined in time periods such as:

$$\delta(t) = \begin{cases} Q & t \in [0, \tilde{t}] \\ O & elsewhere \end{cases} \tag{15}$$

The temperature response must be integrated over the time considered:

$$T(r,t) = \int_0^t \delta(t')G(r,t-t')\,dt' \tag{16}$$

The knowledge acquired by the green analysis just discussed and the linearity of the heat equation allow to determine the temperatures inside the domain for every perturbation possible.

To do that is necessary to perform a convolution between the new source function $x(r,t)$ and the Green impulsive response $G(r,t)$:

$$T(r,t) = x(r,t) \otimes G(r,t) \tag{17}$$

Chapter 5

Thermal Parameters analysis

5.1 Introduction

One of the main goals of this thesis was to get information on the behaviour of thermal parameters in response to laser source input. As a result of a more accurate prediction of the laser-tissue interaction in the target area, the device's reliability would in fact increase.

Temperatures in human tissues strongly depend on factors mostly related to:

- Heat source: depending on the wavelength (such as linear, gaussian etc…) and intensity.
- Observation time: simulation time.
- Thermal parameters: thermal conductivity (k), density (ρ), heat capacity (c_p), which describe how the material behaves under heat deposition.

Thermal factors have a significant impact on temperature evaluations, particularly when determining how human tissue responds to heat. Since they rely on temperature, in vitro or in vivo conditions, and water content, the thermal characteristics of human organs can be challenging to accurately measure. Therefore, it is essential to concentrate on their influence and their values in order to develop a trustworthy, practical, and foolproof model for patient treatments.

Heat capacity represents the domain's ability to absorb heat, whereas thermal conductivity expresses the domain's ability to conduct heat. For the proper understanding of the interaction between the laser and tissue, both are required. However, it is challenging to extract their values from libraries. A list of the values taken from libraries is shown in Table 2.

Tissue	Thermal Conductivity (W/m-K)	Density (g/cm^3)	Specific heat (J/g-K)
Kidney	0.53	Not found	3.94
Fat	0.16	0.85	2.51
Liver	0.52	1.06	3.63
Lung	0.28	0.55	3.71
Blood	0.52	1.06	4
Bone	2.28	1.7	1.59
Muscle	0.42	1.05	3.77
Abdomen	0.55	1.05	3.69
Brain	0.53	1.05	3.69
Skin	0.21	1.0	3.77

***Table 2**- Thermal properties of human organs*

As can be seen from the data in Table 2, they do not offer any justifications for the conditions they were assessing. There is no information about temperature or water content. This underlines the challenge in locating trustworthy numbers, which are required for precise calculations of the organ's thermal responses and consequently for non-damaging patient therapies.

Effective thermal conductivity is the most reliable indicator of a material's identity and performance. Typically, a temperature and signal gradient are used to assess the thermal measurement performance for individual or combined homogeneous/heterogeneous materials. The two primary types of thermal conductivity measurement methods are steady-state methods and transient approaches. These techniques, which are based on the fundamental laws of heat conduction and electrical analogies, are each applicable for a certain class of materials. Since steady-state approaches are mathematically simpler, they have historically been used more often. The difference between steady-state and transient approaches is significant. While steady-state methods are considered to be more accurate than transient methods for assessing dry materials, transient heat transfer methods can directly determine thermal diffusivity.

The steady-state technique records a measurement when a tested material's thermal state reaches complete equilibrium, which is attained when the temperature at each point of the specimen is constant, and the temperature does not change with time. A disadvantage, however, is that it generally takes a long time to reach the required equilibrium. The method employs the use of Fourier’s heat conduction law:

$$\bar{\phi} = -k\nabla T \tag{18}$$

Where $\bar{\phi}$ represents the heat flux [W/m^2], k the thermal conductivity and ∇T the temperature gradient. The solution to the problems with the different steady heat-flow methods is to convert the heat transfer problem to a one-dimensional problem, thus simplifying the mathematics. For the models of an endless slab, an infinite cylinder, or a sphere, the computations alter. Different forms of thermal conductivity measurements can be distinguished by the typical specimen geometry, the measurement system's setup, and the thermal conductivity's magnitude. The guarded hot plate, heat flow meters, direct heating, pipe method approaches, which use the direction of the heat flow, the conservation of the heat flow, and an auxiliary layer having a known thermal property, are used to determine the thermal magnitude of the measuring object. All these techniques require pricey approach equipment because an effective experimental installation system is frequently required.

Perfect thermal insulation, which reduces parasitic heat losses to the environment, is necessary to obtain accurate results, especially for samples with low thermal conductance values. Furthermore, convection shouldn't obstruct heat conduction; this requirement appears to be difficult to meet in liquid materials. Accurately measuring the imposed temperature difference is another issue with steady-state approaches. Typical temperature sensors are thermocouples and resistance temperature detectors (RTDs).

RTDs can have higher parasitic heat losses and are trickier to attach to the sample. Due to temperature sensor errors, achieving high accuracy in practice is difficult and necessitates relatively complicated experimental setups. Nonetheless, the most common and reliable measurement technique is steady state.

The non-steady-state or transient method captures a measurement as the heating process is taking place. Transient sensors are used in the procedure to identify the parameters of thermal conductivity. In comparison to steady-state approaches, these measurements can be made quickly. Because of this, many solutions to the transient heat conduction equation have been developed utilizing one-, two-, and three-dimensional geometries. Different thermal values can be determined during the measuring procedure thanks to the velocity of the method. As a result, the foundation of this method is a signal measurement and an acceptable temperature difference. By assessing the feedback reaction following the transmission of a signal to the specimen for heat creation in the specimen, the transient approach is evaluated. As a result test time is obtained in time intervals of a few minutes or sub seconds. The signal and reaction in the specimen make this approach more suitable for materials with high moisture content. It is frequently possible to substitute a measurement of the temperature as a function of time at just one location on the specimen for the temperature measurements at two opposing surfaces. The hot-wire and laser flash methods are two transient techniques that are frequently used to assess the thermal conductivity of various materials. The hot-strip or disk approach, a variant of the hot-wire method, can be used to evaluate the thermal conductivity and diffusivity of solid nonelectrically conductive materials.

Thus, the key differences between steady state and transient approaches are the thermal conductivity range, the range of material kinds, the measurement period, the measurement precision, the specimen type, and the temperature range.[35]

5.2 Heat Pulse Method

The heat pulse method is a quick way to assess the thermal characteristics of biological tissues in a medical setting.

It has been applied to a variety of substances, including gases, liquids, and biological tissues. For the purposes of this thesis, we solely apply the HPM to research biological tissues at atmospheric pressure and ambient temperatures ranging from 30 to 60°C.

A heat source and a temperature sensor device are required for the heat pulse approach.

The tissue of interest receives the heat energy for a brief period of time, which raises the local temperature. During both the heating and cooling phases, the sensor records the temperature trend.

Thermal characteristics are assessed by utilizing Green's function method to fit the experimentally observed temperature trend to the analytical temperature obtained from the solution of the bio-heat equation.[22]

5.3 Green’s function method

This method is valid for different type of heat sources. In this thesis, we focused on a space dependent gaussian function as follows:

$$q(\bar{x},t) = Q\delta(t) \cdot \frac{1}{(2\pi\sigma_s^2)^{3/2}} \exp\left\{-\frac{r^2}{2\sigma_s^2}\right\} \tag{19}$$

Where:

- Q is the heat power source [W];
- $\delta(t)$ is the Delta di Dirac;
- σ_s is the Gaussian spatial width [mm];
- r is the radial distance from the source [mm];

The thermal response of a system to a heat source different from the Dirac’s one Is the following:

$$T(r,t) = Q \cdot \frac{1}{(2\pi\sigma_s^2)^{3/2}} \exp\left\{-\frac{r^2}{2\sigma_s^2}\right\} * \frac{1}{(2\pi\sigma_t^2)^{3/2}} \exp\left\{-\frac{r^2}{2\sigma_t^2}\right\} \tag{20}$$

Where $(*)$ is the convolution product sign and $\sigma_t = 2kt$. The convolution product between two Gaussian with standard deviation ${\sigma_1}^2, {\sigma_2}^2$ is a Gaussian with variance ${\sigma_1}^2 + {\sigma_2}^2$. Thus we obtain:

$$T(r,t) = \frac{Q}{[2\pi(\sigma_s^2 + 2kt)]^{3/2}} \exp\left\{-\frac{r^2}{2(\sigma_s^2 + 2kt)}\right\} \tag{21}$$

Defining now $t_s : {\sigma_s}^2 = 2kt_s$, we can retrieve the temperature solution as follows:

$$T(r,t) = \frac{Q}{\{4\pi k(t + t_s)\}^{3/2}} \exp\left\{-\frac{r^2}{4k(t + t_s)}\right\}, \qquad t \geq 0 \tag{22}$$

Considering then a source emitting constant power for $t \in [0, \tilde{t}]$, the temperature distribution retrieved would be:

$$T(r,t) = Q \int_0^{min[t,\tilde{t}]} \frac{1}{\{4\pi k(t - t' + t_s)\}^{3/2}} \exp\left\{-\frac{r^2}{4k(t - t' + t_s)}\right\} dt' \tag{23}$$

During the heating transient, for $t \leq \tilde{t}$: through substitutions and variable change we obtain.

$$T(r,t) = Q \int_{t_s}^{t+t_s} \frac{1}{(4\pi k\tau)^{3/2}} \cdot \exp\left(-\frac{r^2}{4k\tau}\right) d\tau \tag{24}$$

Required substitutions:

- $t - t' + t_s = \tau$
- $dt' = d\tau$
- $for\ t' = 0, then\ \tau = \ t + t_s$
- $for\ t' = t, then\ \tau = \ t_s$

$$T(r,t) = Q \int_{0}^{t+t_s} [\dots]\, d\tau - Q \int_{0}^{t_s} [\dots]\, d\tau \tag{25}$$

The temperature equation presents similarities with the complementary error function *erfc,* which is now introduced.

$$\mathrm{erfc}(z) = \frac{2}{\sqrt{\pi}} \int_{0}^{+\infty} e^{-\xi^2}\, d\xi \tag{26}$$

Leading to:

$$T(r,t) = \frac{Q}{4\pi kr} \cdot \left\{ erfc\left[\left(\frac{r^2}{4k(t+t_s)}\right)^{1/2} \right] - erfc\left[\left(\frac{r^2}{4kt_s}\right)^{1/2} \right] \right\} \tag{27}$$

During the cooling phase, for $t \geq \tilde{t}$: as before, through a variable change we retrieve:

$$T(r,t) = Q \int_{t+t_s-\tilde{t}}^{t+t_s} [\dots]\, d\tau \tag{28}$$

$$T(r,t) = Q\int_{0}^{t+t_s} [\dots]\, d\tau - Q\int_{0}^{t+t_s-\tilde{t}} [\dots]\, d\tau \tag{29}$$

$$T(r,t) = \frac{Q}{4\pi kr}\cdot\left\{erfc\left[\left(\frac{r^2}{4k(t+t_s)}\right)^{1/2}\right] - erfc\left[\left(\frac{r^2}{4k(t+t_s-\tilde{t})}\right)^{1/2}\right]\right\} \tag{30}$$

This is the temperature function dependent on time and position valid for the heating transient. This expression will be later exploited to evaluate the analytical thermal response of the built model and its real thermal diffusivity through Matlab codes.

Chapter 6

Thermal Model set up

6.1 Introduction

In order to assist medical staffs in the development of laser thermal therapies, the primary goal of this thesis study was to develop a realistic model that could investigate the thermal response of human tissue over a laser application.
To verify the accuracy of the application, emphasis was given on the investigation of the volumetric range impact of the heat source. In order to determine the viability of the used device, consideration was given to the potential influence of the monitoring fiber over the obtained temperature profiles after the model setup and dimensions had been verified. Lastly, to achieve a more realistic model, analyses were conducted over more complex heat sources. Exploiting the linearity of the heat equation, thus, the heat source was considered as a superposition of different Gaussians.

6.2 Finite Element Method

The finite element method (FEM) is one of the most powerful tools nowadays known to compute approximations of the partial differential equations (PDEs) real solution of space and time- dependent problems, usually describing physic laws. Its huge applicability is related to the excessive complexity of solving PDEs analytically for the vast majority of geometries and problem. FEM instead, thanks to equation’s approximations based on the principle of discretization, is able to overcome this issue. These discretization methods approximate the PDEs with numerical model equations, which can be solved using numerical methods, where the solutions are, in turn, an approximation of the real solution to the PDEs. This numerical tool allows to transform differential equations over a volume to algebraic equation at the discretization points, called nodes.

The usefulness of the method was first recognized at the start of the 1940s by Richard Courant, a German American mathematician. Nonetheless it took several decades before the approach was applied generally in fields outside of structural mechanics, becoming what it is today.

The basic principle of FEM computation is to approximate a general function u with u_h, which is a linear combination of linear basis functions called φ_i, multiplied by coefficients which are suitably tuned to deal with boundary conditions and to minimize the error with respect to the real solution, usually through Galerking Method.

$$u_h = \sum_i u_i \varphi_i \tag{31}$$

A huge benefit of using the finite element method is that it offers great freedom in the selection of discretization, both in the elements that may be used to discretize space and the basic functions. The quality of the solution is strictly related to the number and size of the finite elements exploited to discretize the volume studied: the finer it is, the higher will be the accuracy of the solution. However, this leads to higher computational cost too, which can be decreased consistently by choosing a coarser mesh.

Another benefit of the finite element method is that the theory upon it is based on is well developed due to the close relationship between the numerical formulation and the weak formulation of the PDE. For instance, the theory provides useful error estimates, or bounds for the error, when the numerical model equations are solved on a computer.[6]

6.3 Comsol Multiphysic

Comsol Multiphysics (CM) is a finite element analysis, solver, and simulation software package for various physics and engineering applications, able to couple phenomena and multiphysics. The software facilitates conventional physics-based user interfaces and couples systems of partial differential equations (PDEs).

It presents a Model Builder that includes all the steps in the modelling workflow from defining geometries, material properties, and the physics that describe specific phenomena to performing computations and evaluating the results.

To achieve the objectives of this thesis project, Comsol Thermal and Bio Heat transfer package was chosen as FEM tool. The basic steps for the simulation implementations can be summarized as follows:

1. Geometry build-up.
2. Materials selection.
3. Boundary conditions set up and application of Thermal sources based on the Bio-Heat equation.
4. Mesh definition.
5. Transient analysis.
6. CM result postprocessing.

7. Matlab postprocessing.

6.4 2D Thermal Analysis

Thermal analysis was performed to validate the analytical method based on Green's function, used to reconstruct the biological human tissue parameters and to comprehend the accuracy of the model regarding the influence of those parameters as well as border effect and fiber materials over the retrieved temperatures.

The model simulates the response of the system to a Gaussian heat pulse placed inside a biological medium.

6.4.1 Geometry

The model chosen for the study is a three-dimensional cylinder, created exploiting a rectangle rotating along its axis due to heat symmetric conditions imposed on it. This solution allows a computational optimization.

Simulations were thus carried out in a 2D plane defined by r, z coordinates that describes radial (r) and vertical (z) direction respectively. The symmetry axis coincides with the z-axis. Rectangle dimensions are reported in Table 3.

Name	**Value**
L1	8 [mm]
L2	16 [mm]

Table 3- *Chosen dimensions for the model*

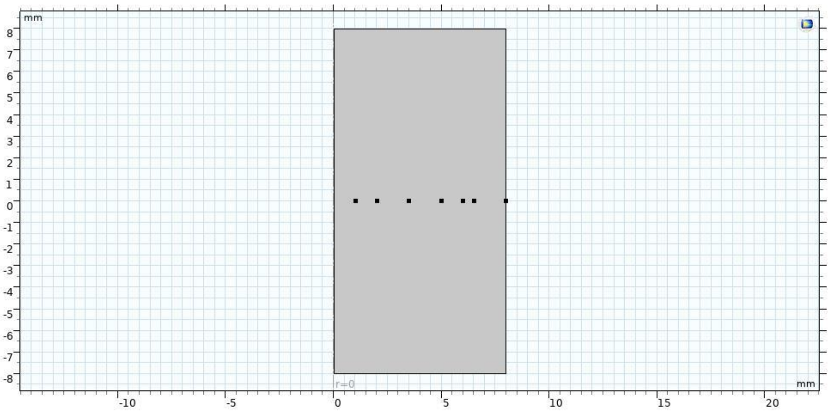

Figure 6.1-*2D model view.*

The choice of optimal dimensions for the model was made upon some critical considerations. The most important objective was to end up with a model as less as possible influenced by the border effect. The choice was made considering:

1. Optimization of the computational cost: a wider volume would have requested indeed too high cost to obtain an as well precise evaluation.
2. Reduction of the difference between the FEM solution and the analytical one: too small dimension model would have differed too much from the analytical solution, retrieved considering an infinite medium. A specific analysis over this topic was later performed to better understand the limit of the numerical solution respect to the analytical one.

6.4.2 Material selection

The objective is to create the most realistic model possible recreating human tissue.

Up to 60 % of the human adult body is water. According to Mitchell, the brain and heart are composed of 73 % water, and the lungs are about 83% water. The skin contains 64 % water, muscles and kidneys are 79 %, and even the bones are watery: 31 %.[31]

Based on these data, the solid model was attributed with water like properties. Simulations were carried out using both H_2O CM material library and temperature constant values:

- Thermal conductivity: $k= 0.56\ [W\ m^{-1}K^{-1}]$
- Specific heat: $c_p= 4186\ [J\ kg^{-1}K^{-1}]$
- Mass density: $\rho= 997\ [kg\ m^{-3}]$

The temperatures outputs coincide in both cases, highlighting the thermal parameters' independency from the induced temperature variations.

6.4.3 Initial and Boundary conditions

To solve the Bio-heat transfer PDE equation, mandatory was the setting of proper initial and boundary conditions. The former was set at 37°C, which represent the human tissue temperature. The latter instead required more considerations: the setting of the correct BC depended indeed on the influence or not of the border effect over the temperature estimations. If that was the case, air flow upon in would have been required to be accounted to be as faithful as possible to the real case scenario. However, the real test, would have been performed on a table too, requiring a proper defined temperature compliant with it. As starting point, thus, the same 37°C organ body temperature was set over the volume boundaries.

The choice made ended up being correct due to the independency of the model from the border effect, analysis shown in detail later on. Thermal isolation condition was set on the rectangle axis rotation.

6.4.5 Mesh creation

FEM tools require a proper volume discretization based on the physics of the problem. The defined sub-element than creates a mesh, that is fundamental in the solving process, as it determines the accuracy of the solution and the computational time as well as CPU memory required. Considering the model set up, a higher refining should have been set next to the heat source where the temperature gradients are wider. However, for sake of simplicity and computational cost, a physical controlled "Extremely fine" mesh was chosen to discretize the volume, with sub-elements of same dimensions. The guaranteed average mesh quality is 0.9617 and minimum element quality of 0.69. The 2D model mesh can be seen in Figure 6.2.

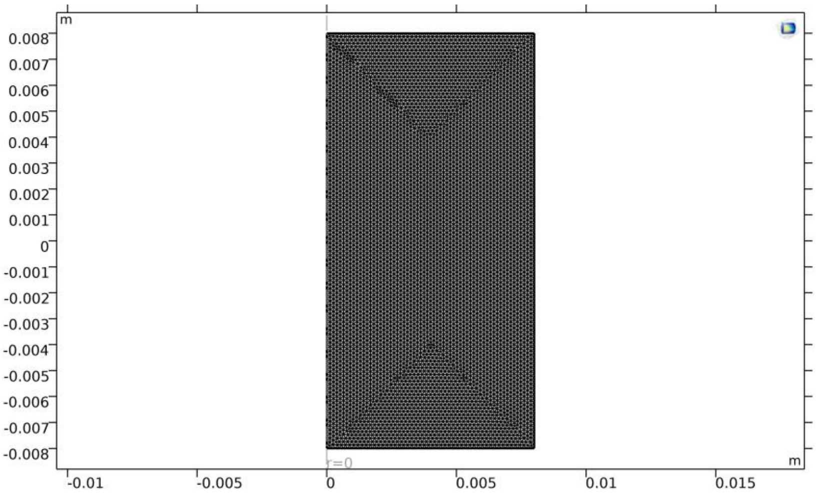

Figure 6.2- 2D mesh.

The goal is to obtain a thermal map highlighting the evolution during both heating and cooling phase of the cylinder. Hence, a 45 seconds simulation duration was established.

6.4.6 Heat source definition

Different heat distributions can be chosen to simulate the laser radiation, depending on the device design and operating principle. The vast array of energy distributions that can be achieved offers remarkable versatility in customising these devices for a given purpose. However, this also makes difficult the selection of the appropriate mathematical expression for the given task. Typically, three different kinds of heat source models are employed:

- The Gaussian model: ideal for high power densities, such as electron beam, laser, and plasma welding. With this model, deep penetration mapping is possible while keeping minimal width.

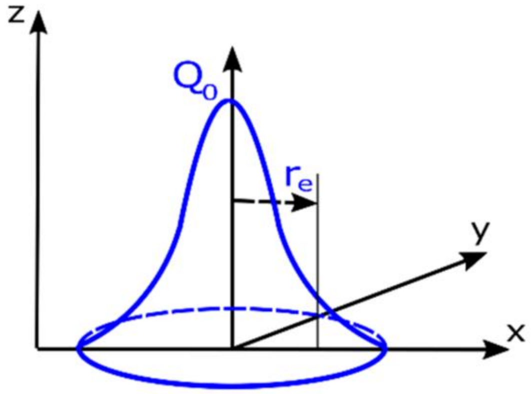

Figure 6.3- *Graphic representation of the Gaussian model.[12]*

- Goldak's model: This model is built of two ellipsoids placed perpendicular to each other.

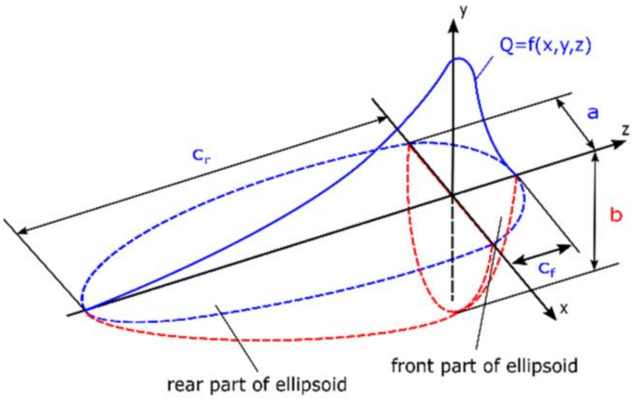

Figure 6.4*- Graphic representation of the Goldak's model. [12]*

- The conical model: usually exploited for high energy densities, i.e., laser, electron beam welding or plasma welding.

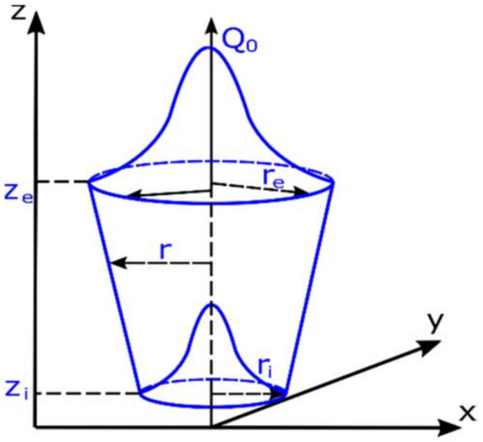

Figure 6.5*- Graphic representation of the Conical model. [12]*

In this Master's thesis, the laser-tissue interaction was investigated considering a Gaussian heat-pulsed source. A Gaussian model is the most common laser energy model used where a symmetric laser irradiance distribution is assumed across the laser beam. In this case the source was distributed over the cylindric volume and pointed at the center r, z= 0 mm. The spatial width was set at 1 mm whereas the emitted power was set at 1 W for a pulse duration of 10 seconds, activated at 2 seconds and stopped at 12 seconds. As said above, the simulations were performed over 45 seconds to consider both heating and cooling transients.

$$G(r,z,\sigma_s) = {}^{1}\Big/_{(2\pi{\sigma_s}^2)^{3/2}} * \exp\left(-\frac{r^2+z^2}{2{\sigma_s}^2}\right) \tag{32}$$

$$P(r,z,t) = Q * W(t) * GG(r,\sigma_s) \tag{33}$$

σ_s: Gaussian spatial width

r: Radial position

z: Position on the z-axis

$G(r,\sigma_s)$: Gaussian function depending on radial position and spatial width

Q: Power emitted [W]

$W(t)$: Time activation function. It is a square function, describing activity of the source throughout the simulation. Figure 6.6

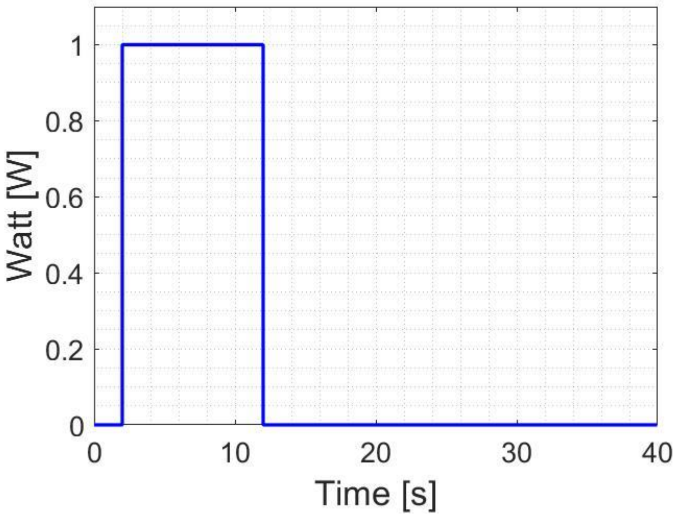

Figure 6.6- *Square function.*

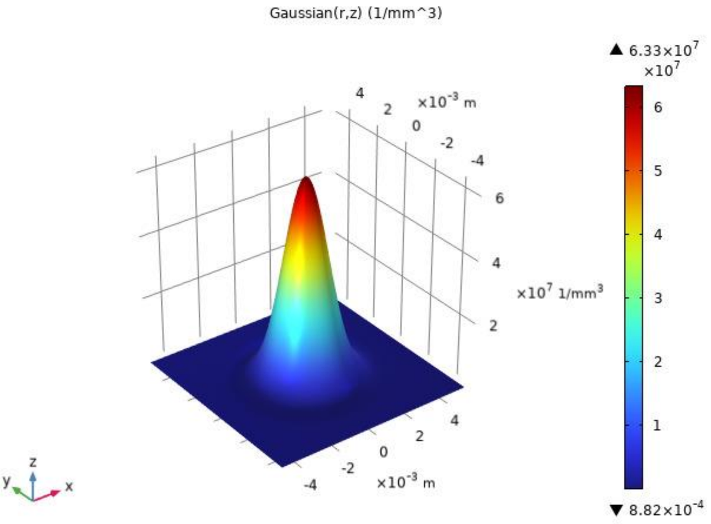

Figure 6.7*- Gaussian source.*

6.4.7 2D Analysis and results

In Figure 6.8 are shown the profiles of the temperature differences between the start and the end of the simulation along the cylinder radius. Temperatures were evaluated at r= 1, 2, 3.5, 5, 6.5 mm. Despite the profiles clearly follow the ones related to the

Gaussian thermal response, they do not respect the heat source time variation. Indeed, as visible in the analysed Figure, the power stops operating at time 10.1 s.

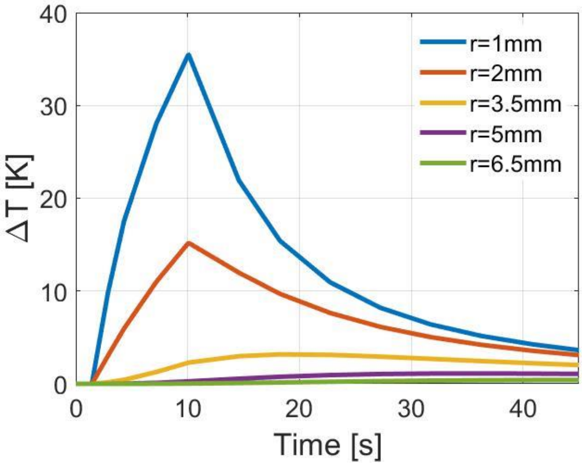

Figure 6.8-Temperatures along the cylinder radius. Low tolerance.

This phenomenon was deeply investigated since no temperature's outlines could be considered valid in these conditions. Employing the analytical solution retrieved from Matlab scripts, we understood the entity of the error made.

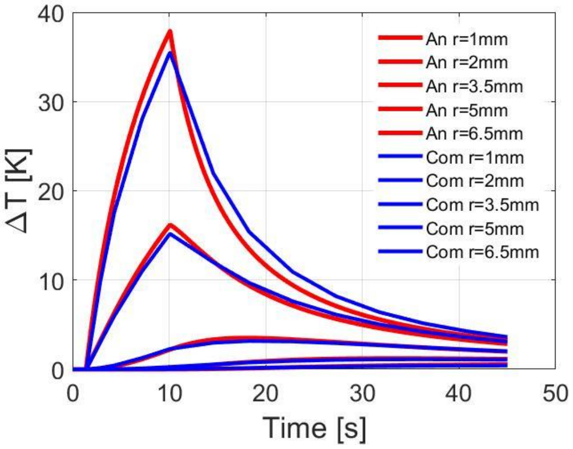

Figure 6.9-Comsol- Anlaytical temperature comparison. Low tolerance.

Figure 6.9 demonstrates that the issue extended beyond the source's incorrect operating time. Discrepancies of 2°C were found indeed by inserting the Comsol simulation's retrieved starting and ending times into the analytical solution. Additionally, appears to be present a difference in the temperature increase velocity. The hypothesis made was that the CM source's time variation reduction also caused the power to increase parabolically.

A study on tolerance was conducted in order to evaluate this problem.

To achieve convergence, the relative and absolute tolerances were gradually reduced.

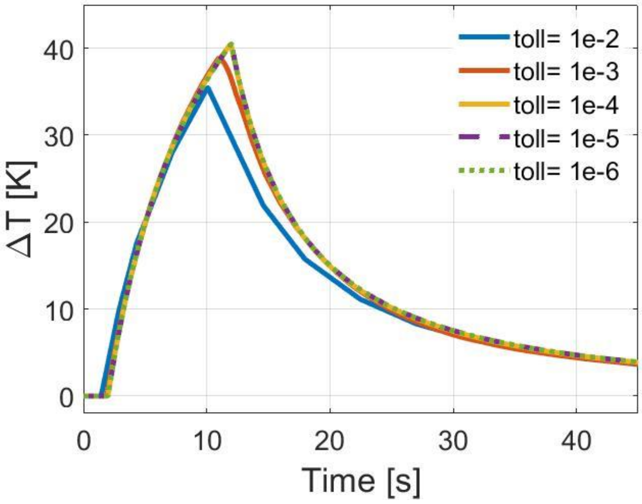

Figure 6.10- *Tollerance study.*

Figure 6.10 highlights the results obtained. Convergence is reached at relative tolerances equal to 1e-4. However, to obtain more precise evaluations, a tolerance of 1e-6 was chosen for all the next simulations.

Having chosen the correct time-solver set-up, new temperature evaluations were retrieved.

The profiles clearly follow the ones related to a Gaussian thermal response. Furthermore, the derived values show physical meaning since they are higher close to the source whilst lower toward the cylindrical border. Interesting is the curve at r= 5 mm, where the temperature difference remains always below 1.5°C, allowing us to hypnotize the small influence of the border effect on the built model.

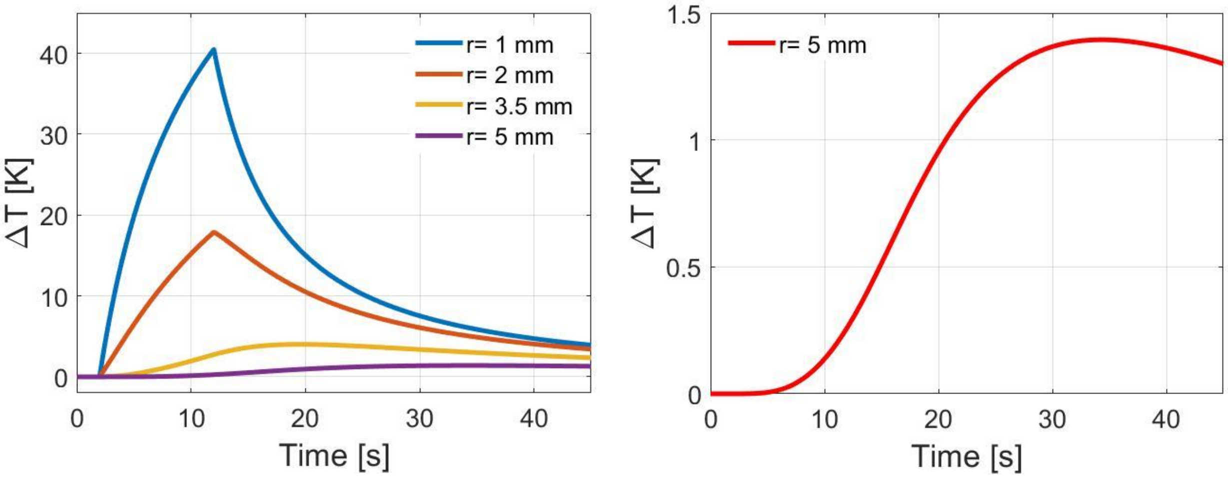

Figure 6.11-*Temperatures along the cylinder radius. 1e-6 tolerance.*

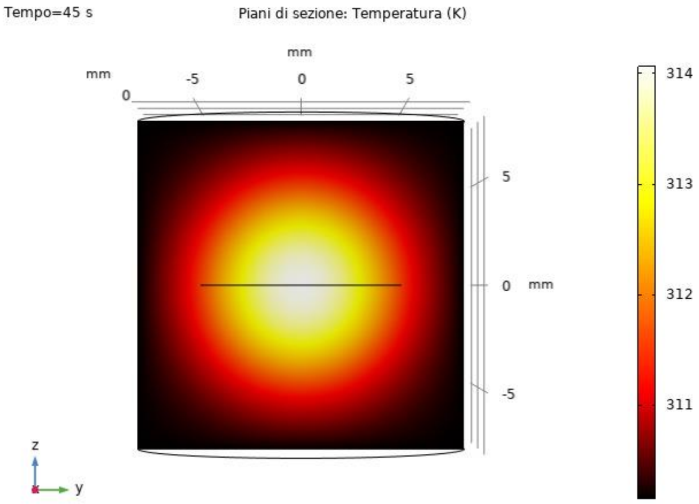

Figure 6.12- *Temperature map at t= 45 s, at r=1 mm.*

Thanks to the Matlab codes, able to provide the analytical solution, it was later computed the error in the CM temperature evaluations. As shown in Figure 6.13, the discrepancies are negligible, even close to the source where gradients are higher and lead to greater errors related to the finite element discretization. The error along the cylinder radius is below 1 %, except at r= 5 mm where it reaches 5 %, which is still acceptable.

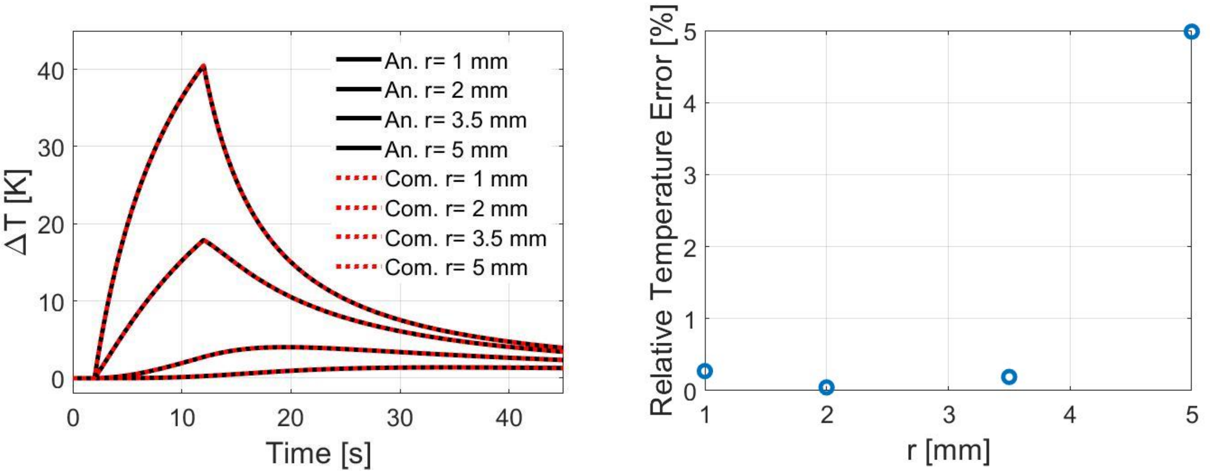

***Figure 6.13**- Relative Temperature Error.*

Afterward, to deeply investigate the possible influence of the border effect and the On-power time over the model, some tests were performed.

- **Cylinder dimensions Parametric sweep**: from L1= 1.5 mm to L1 =192 mm.

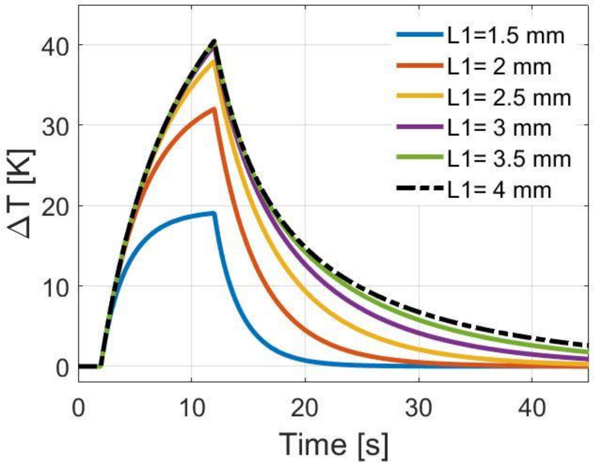

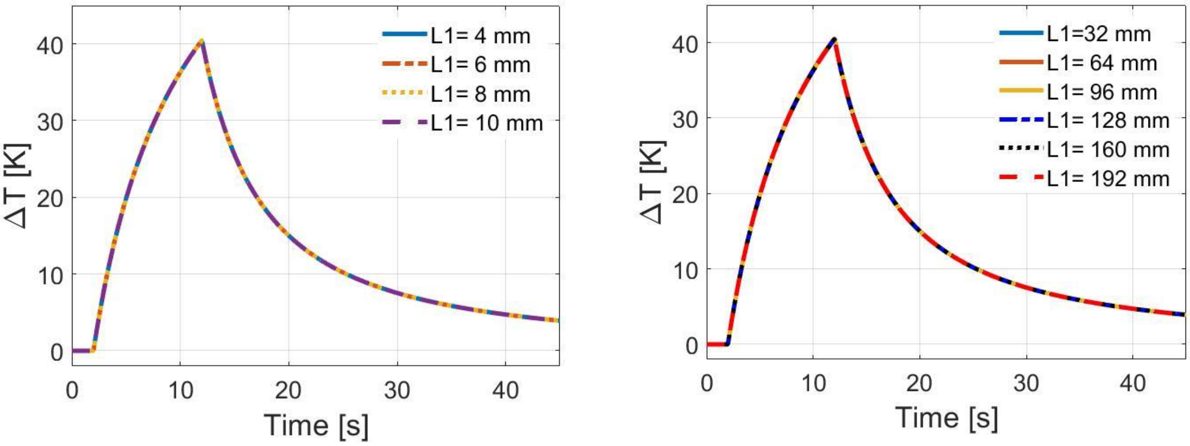

Figure 4*- Dimensions effect over temperature estimations.*

The temperatures were retrieved at 1 mm from the heat source for every configuration. As expected, the border effects the model when the evaluation point is very close to the border itself, so for L1 = 1.5, 2, 2.5 mm. The presence of the Dirichlet condition of T = 37°C on the border indeed influences the temperature behaviour, whose growth rate is slow. Temperatures reached before power shutdown are lower in these cases. This analysis expresses the limit between the numerical solution and the analytical one, obtained considering and infinite medium.

The border, however, appears to be irrelevant even for a small cylinder dimension like L1 = 3.5 mm where correct temperature profiles are already obtained. No differences can be found between the other configurations.

- **On-power time Parametric sweep**: from five seconds to twenty seconds.

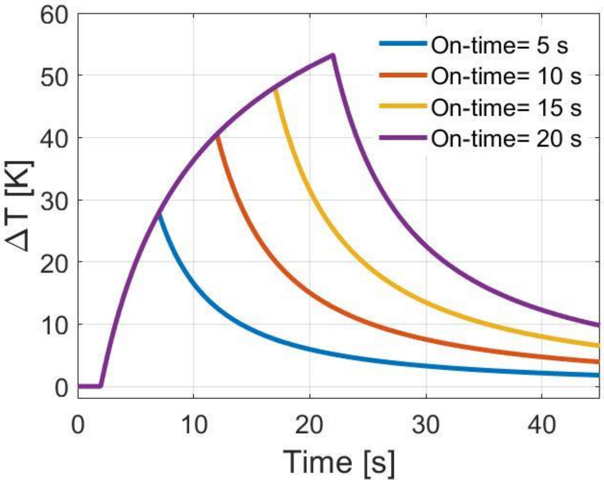

Figure 6.15- *On-power time effect.*

Evidently, by increasing the source time activity, the difference temperature values obtained must be higher, as shown in Figure 6.15, since higher heat is absorbed. Interesting is noticing that with 20 seconds of 1 W power application, cell damages can be induced, since temperature in the order of 60°C is reached. However, important is to highlight the fact that in every configuration, the growth' slope is exactly equal, emphasizing the lack of influence of the parameter over the physic of the model. These results prove the independency of the established model from the border effect and the on-power time which was the primary objective.

6.4.8 Real Thermal properties reconstruction

Exploiting HPM previously seen in Chapter 5, the real thermal properties were reconstructed. A comparison with the constant ones initially employed for the thermal model was conducted. Figure 6.16 depicts the entity of the differences between the real thermal diffusivity values along the cylinder radial direction and the one used for the simulations. The obtained values highlight the correctness of the implemented model since no evident discrepancies can be noticed. Thermal diffusivity values are distributed in a $0.04x10^{-7}$ [m^2/s] span.

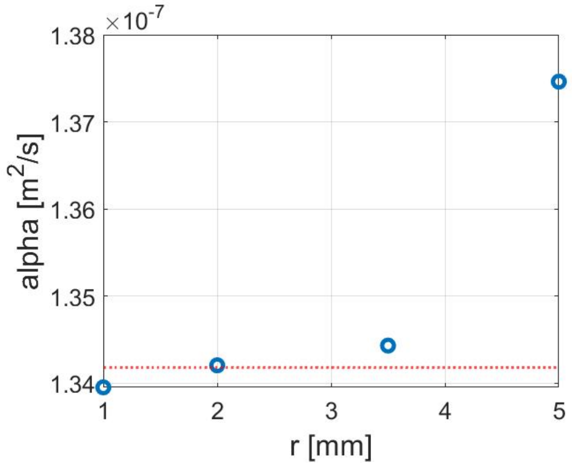

Figure 6.16- Thermal diffusivity comparison with employed one.

6.4.9 Observation and conclusion

The model created for thermal simulation is corrected, since it respects the desired independency from the border effect and fits exactly the analytical solution. For these tests, the 2D axisymmetric model allows a high computation efficiency and good accuracy for what regard temperature evaluations considering a high tolerance setting. In fact, given lower tolerances, for positions closer to the source, $r < 3$ mm, the effect of the discretization errors of the finite element method plays a significant role, since the discrepancy with the analytical solution is wider.

In conclusion, the choice of temperature sensing point for the evaluation of the analytical method turns out to be 1 mm, as it guarantees for high tolerances, no discrepancy from the analytical solution. The model was thus validated.

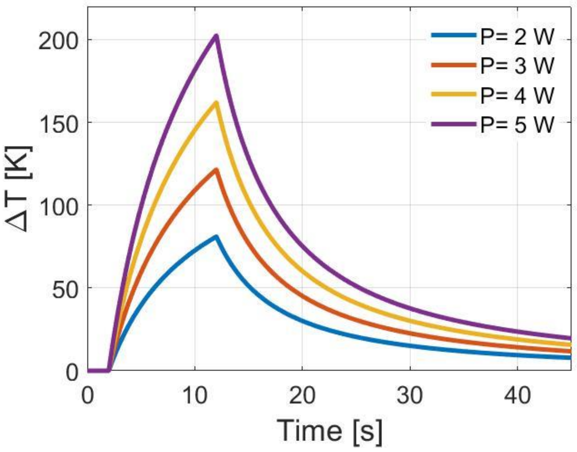

Figure 6.17*- Power intensity analysis.*

Figure 6.16 presents an analysis of the power intensity, applied on the model. With same treatment duration, different temperature rises are induced to the medium. Employing small power already lead to cell damaging, with carbonizations even for intensities ≥ 3 W.

Chapter 7

Fiber material and position effect

7.1 Introduction

The model was built considering a cylinder heated by a laser emitting a Gaussian-like power over the volume domain. The realistic temperature monitoring would require the presence of another fiber close to source one. The best possible collocation of the monitoring fiber should be around maximum r =1 mm (considering the source one at the volume center: r = 0 mm), due to experimental and mechanical feasibility. The position of the monitoring fiber, to obtain the most realistic possible temperature response and effect of the tissue, should be as close as possible to the heat source.

Is the monitoring fiber distorting the temperature evaluations along the cylinder radius? Are the fiber materials influencing the temperatures? How strong are the distortions?

The possible influence of the monitoring fiber was thus investigated. A new model was required since symmetry could not be exploited anymore.

7.2 3D Thermal Analysis

To evaluate the prominence of the monitoring fiber in the temperature profiles, two new models, shown below in Figure 7.1, were implemented.

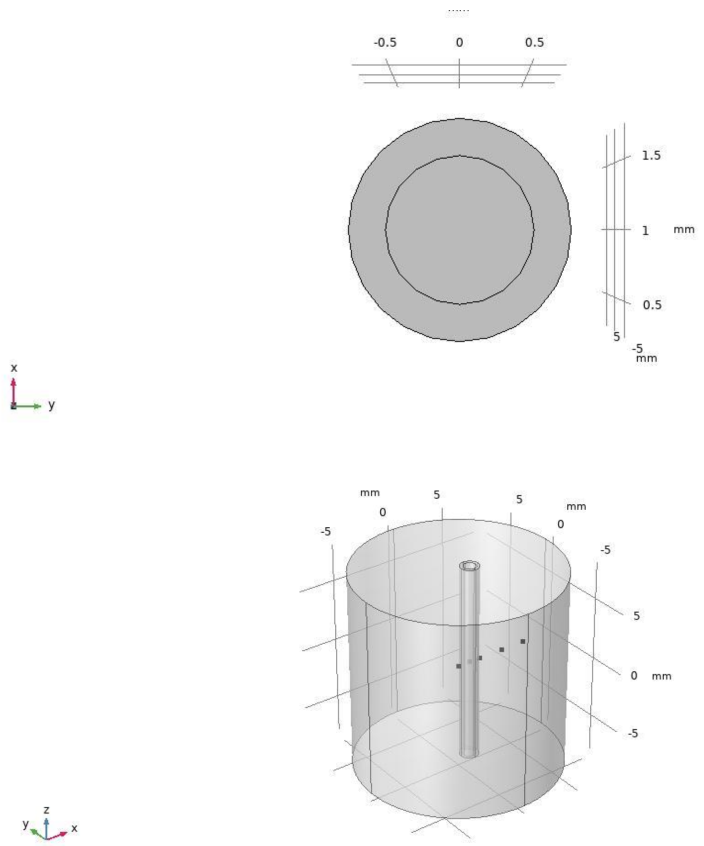

Figure 7.15- 3D model with first fiber configuration.

- **First configuration**: the fiber was inserted in the previous model as a cylindrical air volume with a 1 mm diameter, covered by glass coating, 0.25 mm thick. The air cylinder diameter was set considering the worst-case scenario.
- **Second configuration**: this model represents the most realistic between the two created. The first configuration was upgraded inserting the glass fiber volume, of a 125 micrometres diameter, inside the cylindrical air volume of 1 mm.

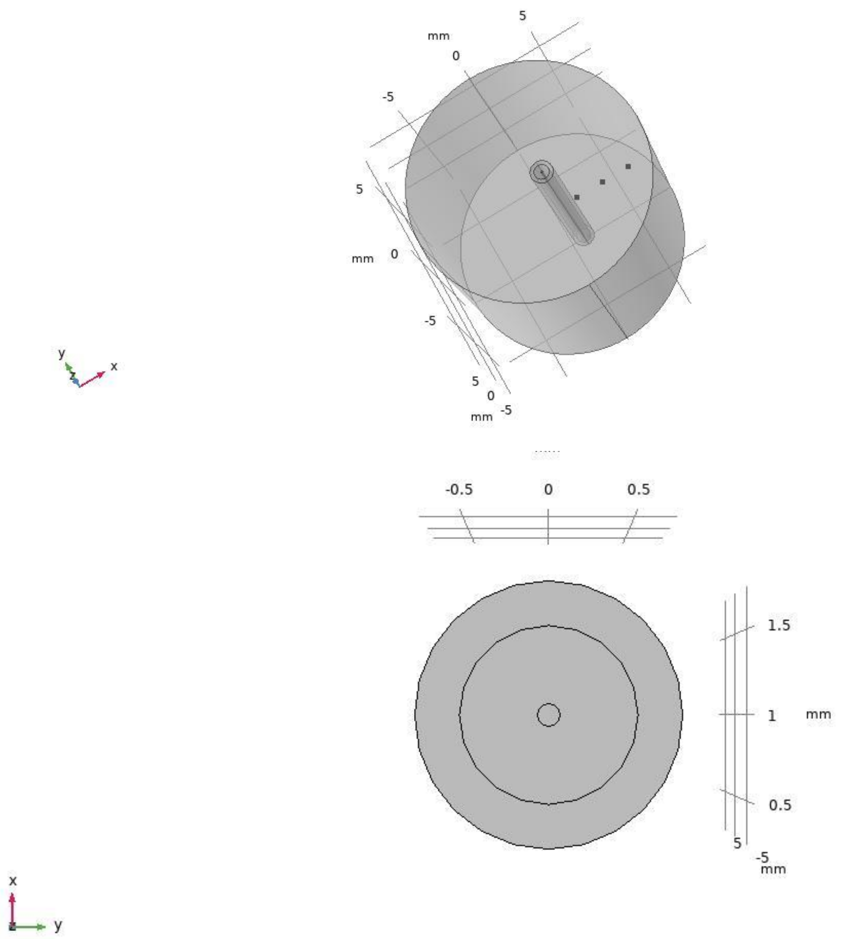

__Figure__ 7.2-3D model with second fiber configuration.

In both settings, the fiber was positioned at a 1 mm distance from the heat source, representing the radial limit for monitoring. The type of glass chosen for the fiber was the Silica one, whose parameters and characteristics were retrieved from CM material library.

The initial and boundary conditions necessary for the Bio-Heat thermal equation were set following the same reasoning considered for the 2D axisymmetric model, as well as tissue parameters and heat source.

7.3 3D Mesh setting

For the 3D model a different discretization procedure was pursued. A tetraedric unstructured mesh user defined was chosen. For the fiber volume an “Extremely Fine” discretization was set, whereas in the rest of the volume a much coarser one was selected. The reasons behind this setting are related to the geometry of the fiber, characterized by very small dimensions. The proximity of the fiber to the source furthermore allows smaller size sub-elements creations in the region where the temperature gradient is expected to be higher. This set up should decrease the effect of the finite element discretization over the temperature evaluations.

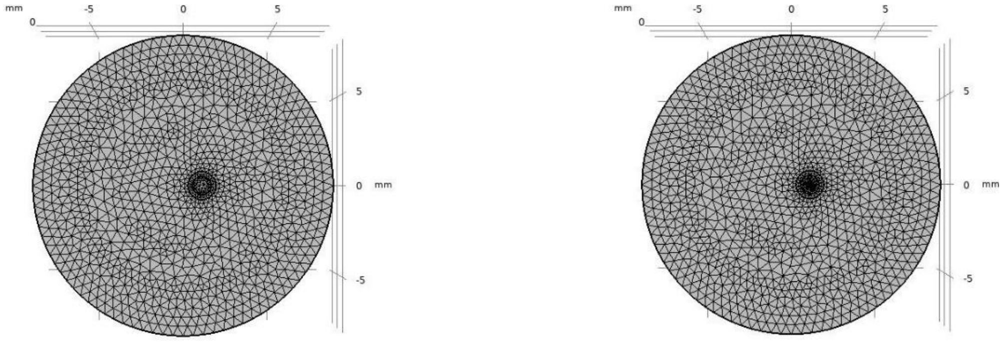

Figure 7.3- 2D mesh maps for the two fiber settings.

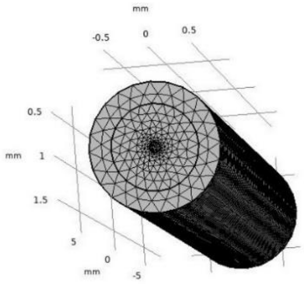

Figure 7.4- Fiber second configuration zoom.

7.4 3D Fiber Results

Firstly, to corroborate the validity of the 3D model, a comparison with the analytical solution was performed. Figure 7.5 shows discrepancies mostly for r= 1 mm, close to the source, where gradients are higher, and the influence of the FEM element discretization is greater. The 3D model would require much more computational time to reach the same accuracy as achieved by the 2D model. Figure 7.5 shows discrepancies in the order of 2°C respect the analytical solution retrieved from Matlab codes. This is probably related to the chosen mesh, which appears to be not perfect. A higher mesh refinement close to the source should have been employed, to better compute the high temperature gradients. The 3D model requires much more computational time to reach the same accuracy. Tolerance was set equal to 10^{-6}. Simulations with lower tolerances showed in fact the same problems experienced in the 2D axisymmetric analysis.

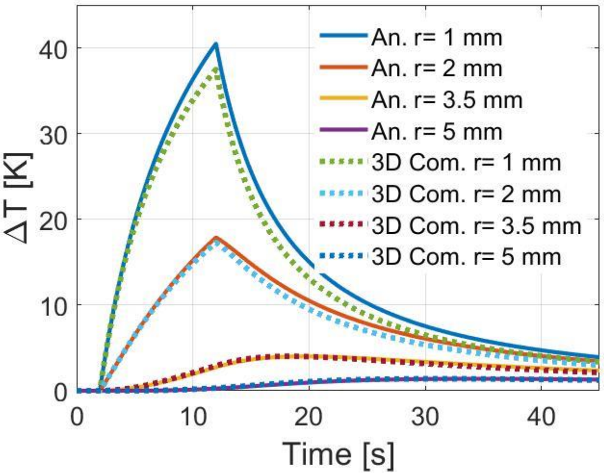

***Figure** 7.5- temperature comparison between 3D model and analytical solution.*

Afterward, temperature profiles over the simulation time were acquired along the cylinder radius, respectively at r = 1, 2, 3.5, 5 mm.

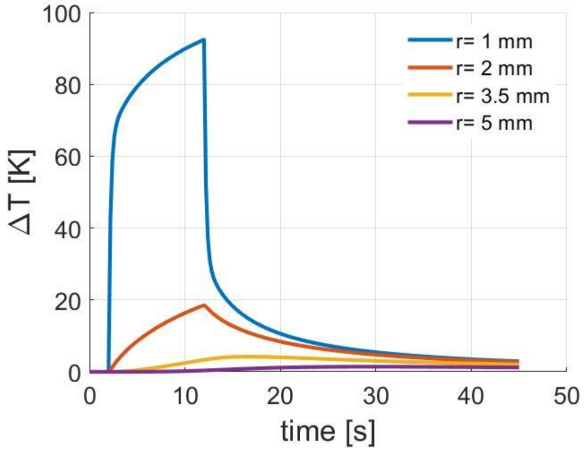

Figure 7.6*- Temperature profiles with fiber at r=1 mm.*

Compared to the 2D analysis, in Figure 7.6 stands out the temperature outline at r =1 mm, the fiber centre. Here, the temperature soars to levels almost equal to 90°C, emphasizing the significant impact of the fiber composition on temperature predictions.

This could result in seriously erroneous and exaggerated assessments of the laser's impact on tissue. A maximum temperature of 92.4°C, as sensed by the monitoring system would cause cell necrosis. However, the real temperature would be within the acceptable range for cell survival of 40°C.

It would be interesting to validate the phenomena in order to develop a suitable scale that could compare the two circumstances side by side right away. However, since nothing can be measured without a monitoring system, which has a significant impact on the output results, it is unfortunately difficult to validate this occurrence through actual trials. The values along the radius, close to the fiber, seem unchanged, as can be grasped in Figure 7.7.

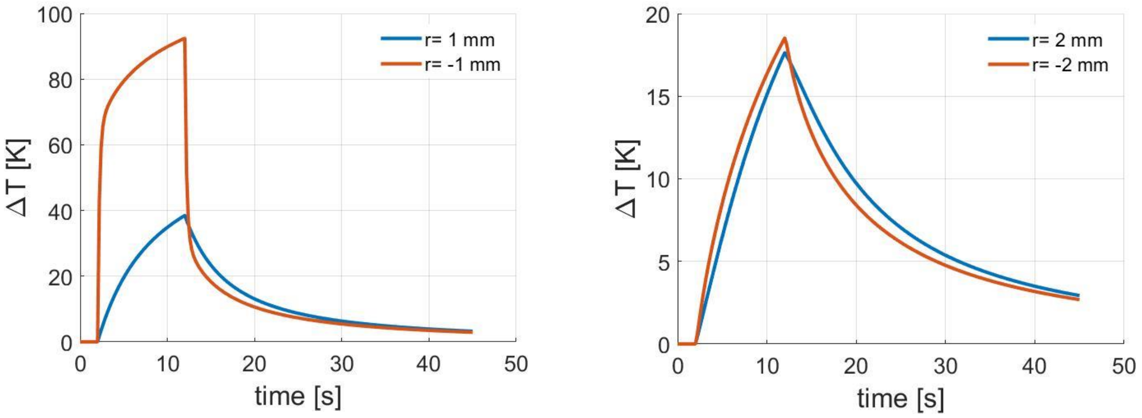

***Figure** 7.7- Temperature comparison in the same positions at different conditions: fiber and no fiber.*

This phenomenon is physically traced back to the material properties of the fiber. Indeed, the air conductivity is much lower than water and glass ones. Temperature difference in that volume is than much higher. However, being the conductivity lower, thus its capability of conducing heat is low, the velocity of the temperature ramping should be much smaller than the one retrieved. This could be possibly induced by the huge effect of the 0.25 mm Silica glass coating, whose thermal conductivity is twice as large than the water one.

Specific heat and density properties instead have lower impact over the temperature since their effect tend to compensate. Bio-Heat thermal equation indeed clearly state the inverse proportionality of the temperature gradient on the thermal conductivity and the density, specific heat product.

	Thermal conductivity [W/m/K]	Specific heat [J/kg/K]	Density [kg/m^3]
H_2O	0.56	4186	997
Glass	1	700	2200
Air	0.026	1000	1.293

Table 4- *Material properties*

Results, highlighting what described above, can be observed in Figures 7.7 above and in the temperature maps showed in Figure 7.8, 7.9, where the distortion induced by the fiber at t= 12 s is evident.

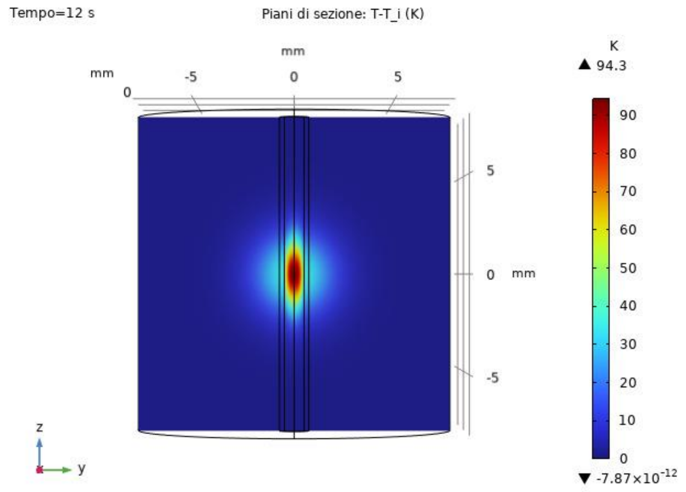

Figure 7.8- *Temperature Map at r=1mm, fiber centre.*

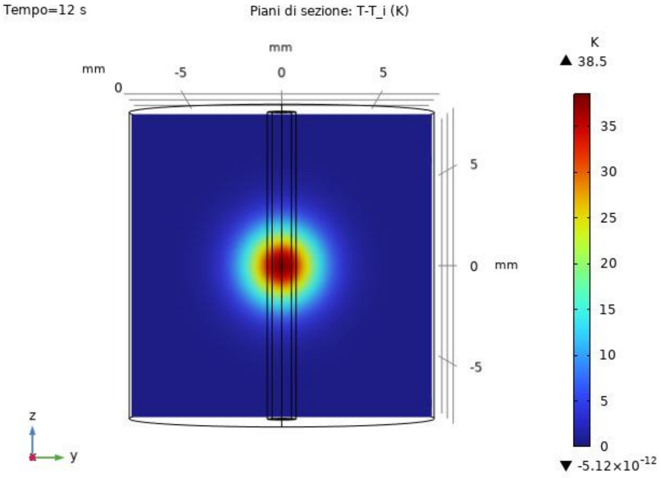

Figure 7.9- *Temperature map at r= -1mm, No fiber.*

Instead, In Figure 7.10 is shown the temperature profiles at r =1 mm for fiber 1 and fiber 2 settings.

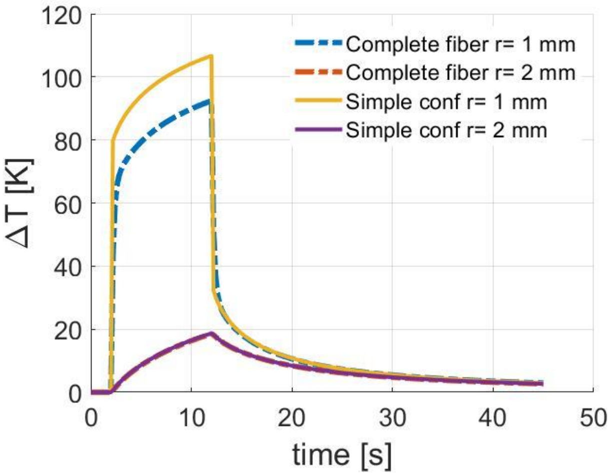

Figure 7.10- *Temperature at r=1 and 2 mm for fiber 1, 2 settings*

According to what explained before, regarding the influence of the fiber material, here can be seen how the lower presence of air volume in the second configuration, and therefore the higher glass volume, lead to a maximum temperature gradient lower than the one retrieved form configuration 1. Steeper temperature increase was however expected in the second fiber setting, due to the greater capability of the glass to conduct heat. This aspect cannot be grasped by Figure 24, where the ramp outlines are parallel. This could be related to the very small dimensions of the fiber, 125 micrometres thick. Configuration 1 maximum temperature retrieved is 106.7°C, compared to configuration 2's one which is 92.4°C. An overestimation of around 12°C respect to the more realistic configuration is thus present when evaluating the temperature in r= 1 mm.

For the simulations, setting number one was chosen due to its higher temperature discrepancy with respect to the realistic case (no fiber). Hence, the worst-case scenario was selected.

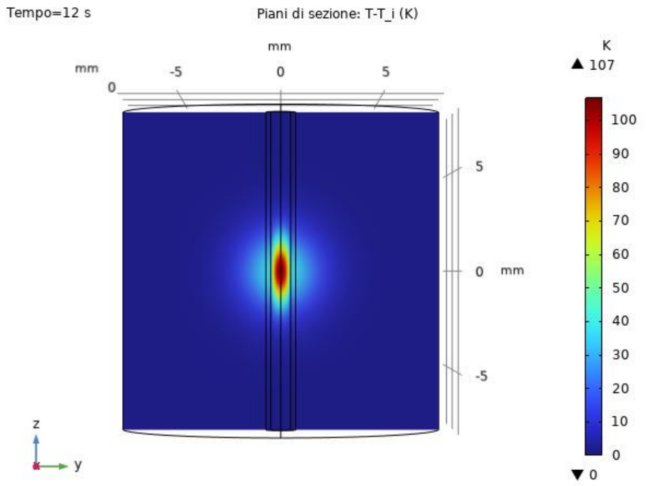

Figure 7.11*- Temperature maps for fiber 1 configuration.*

Figure 7.11 shows the temperature map at r= 1 mm for fiber 1 configuration, were the distortion induced by the fiber is clearly visible. However, apart from the output values, no difference can be grasped respect to the second fiber configuration.

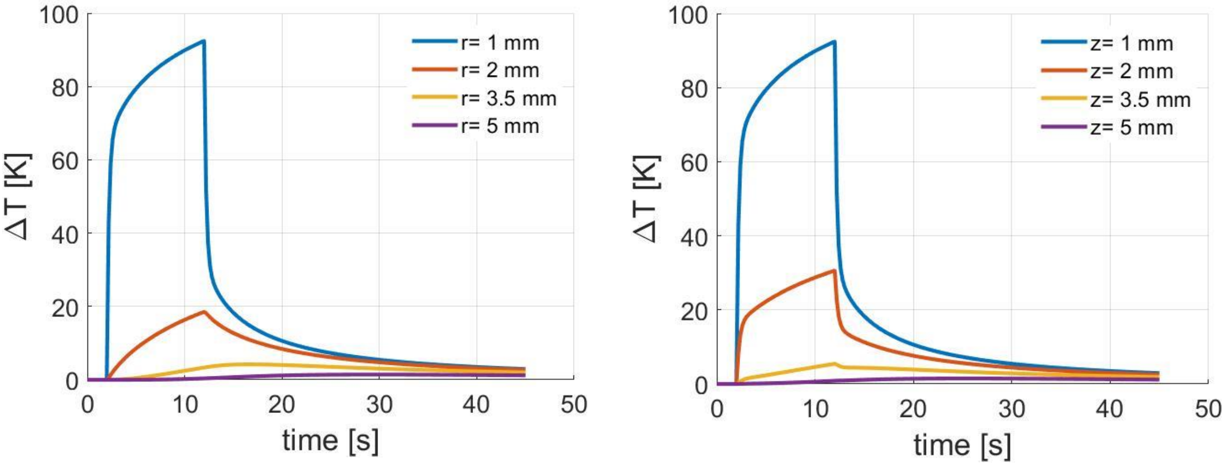

Figure 7.12*- Fiber influence. comparison between radial temperature and temperature retrieved along fiber axis.*

Figure 7.12 allows a better comprehension of the entity of the of fiber distortion. It is cleatly visible at z= 2, 3.5 mm how the presence of air volume changes the growth rate of the temperature profile during the heating transient, leading to values largely higher than expected, even at positions where the influence of the heat source is already modest. At the start of cooling transient instead, temperature steps are perceivable, taking place in fraction of seconds, before following the temperature exponential decrease common to the gaussian response.

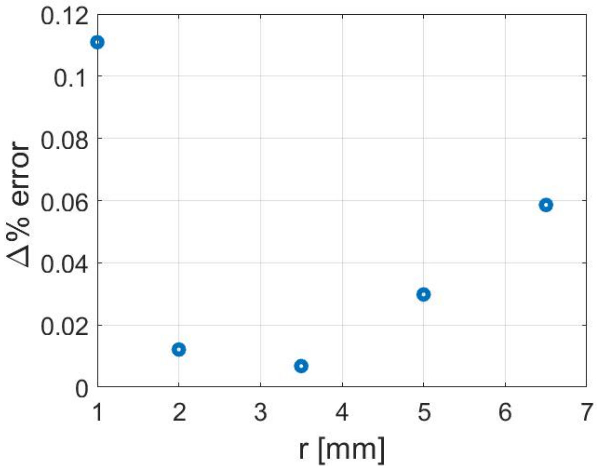

***Figure 7.13**- Error profile with irradiation and convective flux implementation.*

Finally, due to possible reduction of the temperature estimation, the potential impact of surface-surface irradiation and the convective flux of the air flowing inside the fiber was investigated. However, the inaccuracy on the temperature evaluations is mere, as is plainly shown in Figure 7.13. Thus, the chosen model will not account the presence of irradiation between surfaces and air-convective flow for the sake of simplicity and CPU time saved, due to its mere impact.

7.5 Fiber position analysis II

Laser thermal therapies aim is to induce necrosis to cancerous cells due to excessive heat. It can be achieved with temperatures around 60°C.

Hence, we are interested in knowing the source thermal effect close to its origin and application point. For this reason, the fiber was set at 1 mm radially from the source origin. Nonetheless, it was appealing the investigation of the thermal response even in further position, to understand the amount of volume thermally influenced by the source and the fiber distortion entity in its surrounding. Both of them, in order to achieve high treatment precision and measurement accuracy, should be as small as possible. So far, the model showed that huge temperature gradients are obtained just close to the source, whilst mere ones are visible further from it. The maximum temperature gradient is found at r = 1 mm and is equal to 40.5°C, which represent a safe-temperature range for cell survival.

Fiber insertion, necessary for monitoring, however, leads to a huge profile distortion, with soaring temperature equal to 106.7°C for the fiber configuration 1. This temperature estimation is largely overrated respect to the real case. Therefore, the fiber hugely influences the model thermal response.

Based on this knowledge, a study concerning its influence over the entire model, so positions close to it, was carried out.

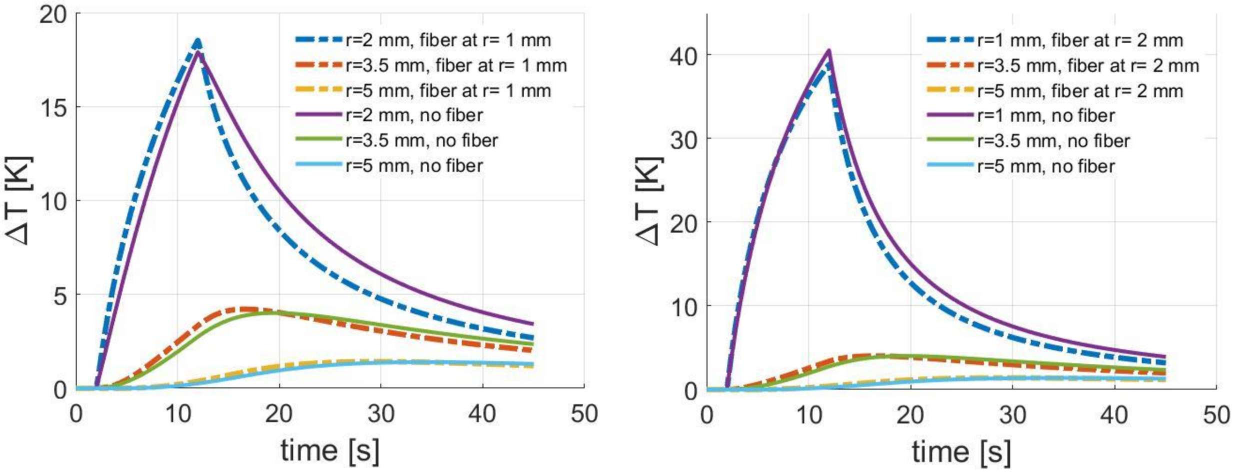

Figure 7.14- *Fiber effects on temperature profiles when positioned at r=1 and 2 mm.*

As can be seen in Figure 7.14, the fiber presence alters the temperature outline in its centre but has negligible influence over the outside positions. The higher effect is witnessed during the cooling transient at the fiber border when the latter is positioned at r = 1 mm. However, in the other cases, the temperature profiles perfectly match, even in the fiber border positions. The analysis made, allowed to verify that the monitoring fiber does not distort widely the surrounding volume temperatures, with mere differences that can be considered negligible. Figure 7.15 pictures temperature evaluations at r= 3.5 mm at three different settings: fiber positioned at r= 2 mm, at r= 1 mm and no fiber. It is evident furthermore how the discrepancies from the expected profile are very small and related merely to the heating and cooling transients.

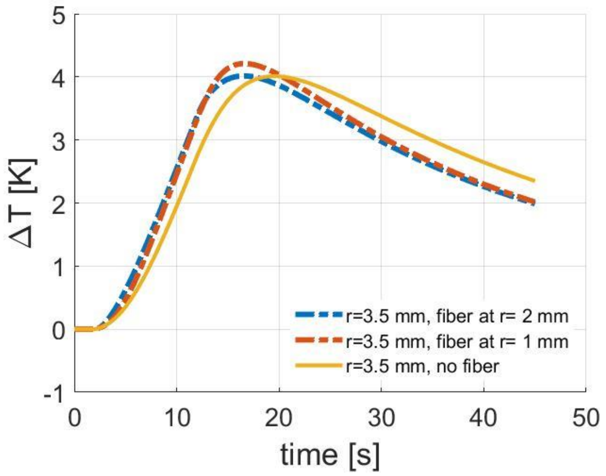

***Figure** 7.15- Temperatures at r= 3.5 mm in three different settings.*

Figures 7.16, 7.17 describe the temperature behaviour for fiber positioned at 2, 3 mm respectively. In the former setting, the fiber centre position temperature follows the same behaviour seen previously. The temperature rockets up doubling the temperature value retrieved without the fiber presence. Maximum values at r= 2 mm is close to the one obtain without fiber at r= 1 mm. Interesting is noticing that for the fiber positioned at 3 mm, the material effect is very low. That is due to the low temperature gradient measured at 3 mm in the model without the fiber. We are at huge distance from the source, so the temperature variation is mere and the effect of the air on the temperature gradient is inferior.

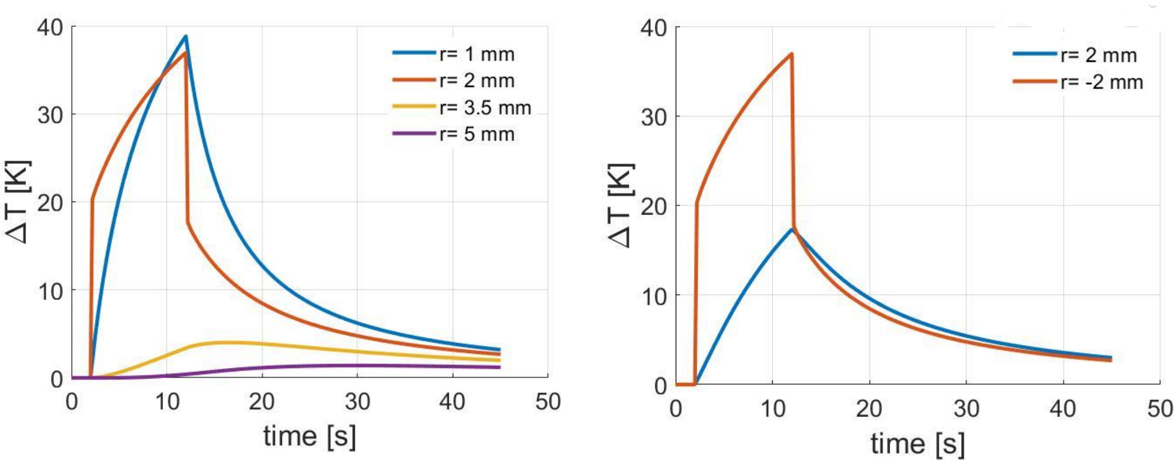

Figure 7.16*- Temperatures with fiber centred at r=2 mm.*

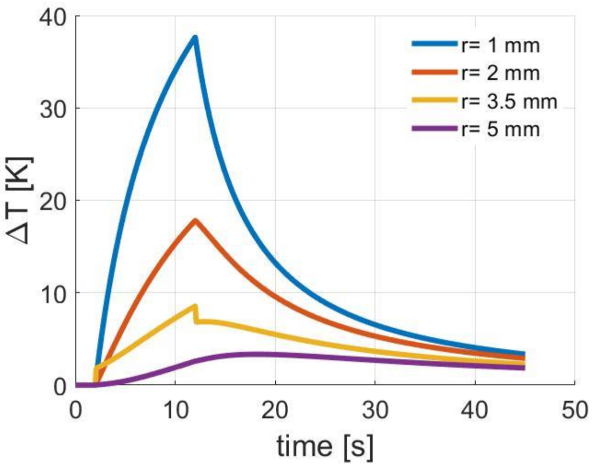

Figure 7.17*- Temperatures with fiber centred at r=3 mm.*

Chapter 8

Delivery system

The Laser heat source has variety of way of being expressed depending on the laser function and objective. Huge differences are present when considering different types of optical fibers. The intensity of single mode fibers, characterized by low diameters, is generally expressed through a Gaussian shape, whereas multi-mode fibers one is much more complex.

Moving to other work fields, i.e, welding, to simulate the propagation of the laser different techniques can been employed. As seen in Chapter 4, heat source definition ranges from the gaussian model, Goldak's model and the conical one.

Hence, in this chapter of the master's thesis, an analysis over the Gaussian delivery system was performed exploiting the linearity of the heat equation to obtain a more realistic heat source definition.

8.1 Introduction

The simulations previously performed utilized a general volumetric gaussian distribution with fixed standard deviation and power variating on time, applied at the medium centre.

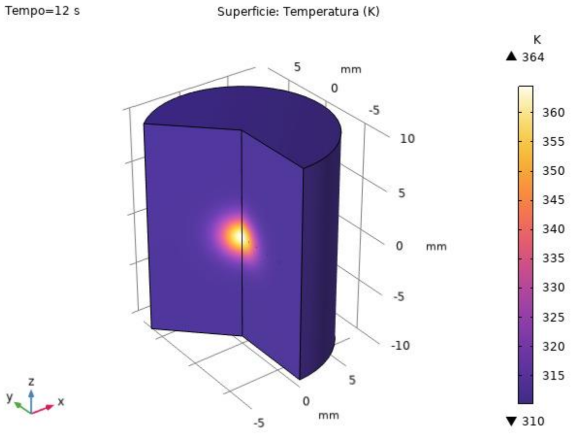

Figure 8.1- Volumetric temperature with gaussian heat source.

Figure 8.1 shows the volumetric temperature response to the gaussian like heat source. The image shown comply with the source definition, which describes an exponential variation over a spheric volume.

In real life operations, the radiation intensity expressions are much more complicated. Furthermore, the intensity should follow the general cone distribution, as depicted in Figure 8.2. Hence, gaussian distributions with parameters depending on vertical direction (z): standard deviation increasing along z, whilst power exponentially decreasing along it.

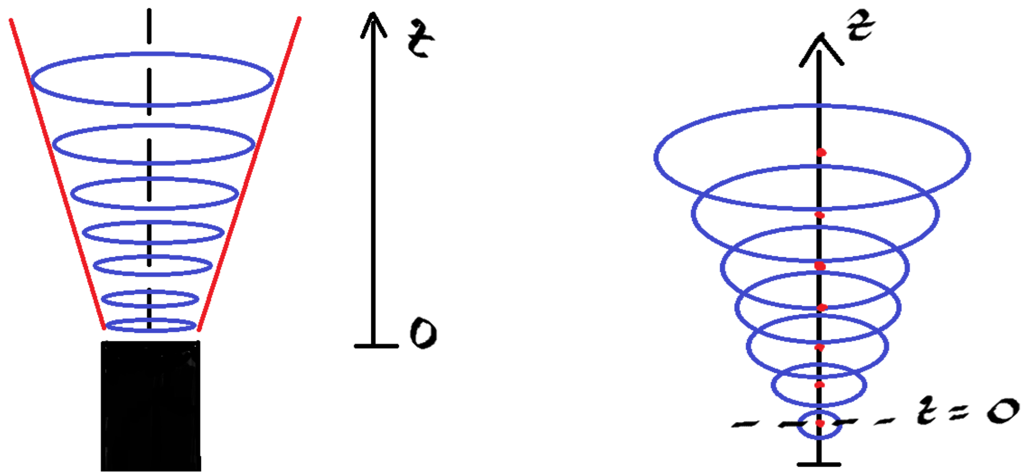

Figure 8.2- Heat source propagation over z-axis.

8.2 Gaussians simulations

Exploiting the linearity of the heat equation is possible to consider the source as a summation of functions. The temperature response, as explained in Chapter 4, can be then evaluated as a convolution of the green function response.

8.3 Summation of two Gaussians

Firstly, we studied a simple case, analysed through Matlab software, where the source has been defined as a summation of two Gaussians positioned at different points z_0 as follows:

$$G(x,y,z) = {}^{1}\Big/_{(2\pi{\sigma_s}^2)^{3/2}} * \exp\left(-\frac{x^2+y^2+(z-z_0)^2}{2{\sigma_s}^2}\right) \qquad (34)$$

Where z_0 are points along the z-axis.

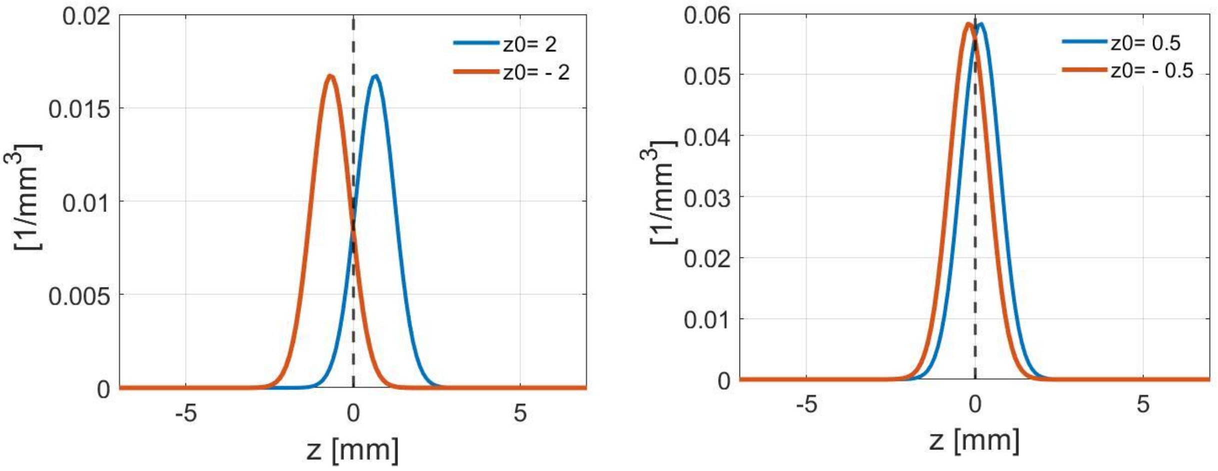

Figure 8.3- *Gaussian shape variation along z, z0=-2, 2 mm and z0=-0.5, 0.5 mm.*

Figure 8.3 depicts two gaussian functions along z-axis described as above, positioned at z_0= -2, 2 mm and z_0= -0.5, 0.5 mm respectively.

For the simulations, the total power desired has been halved between the two.

The choice of the Gaussian functions, mainly related to its centre z_0, plays an important role in the results outcome. As visible from Figure 8.3, depending on the choice of the Gaussian centre, the total heat source function, computed as the sum of the two initialized, can be cancelled or not. To obtain a realistic source thus, a correct tuning of the Gaussian function position is required.

Matlab simulations were performed focusing on this aspect, variating from z_0= 2 mm to z_0= 0.001 mm.

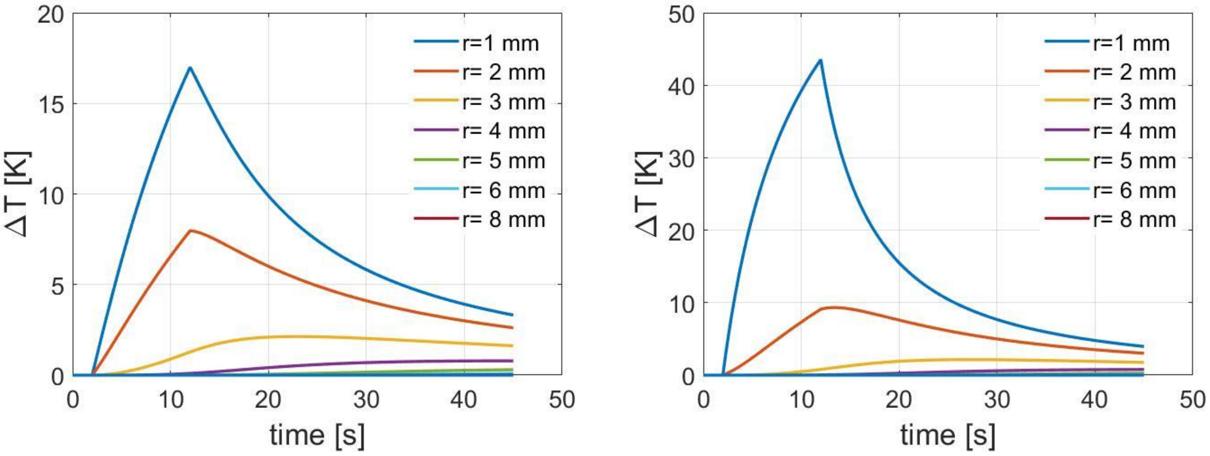

Figure 8.4*- Gaussian summation response analysis depending on z0: z0=2 mm and z0=0.001 mm.*

Figure 8.4 portray the result obtained at specific positions inside our cylinder domain, where r is computed as:

$$r = \sqrt{x^2 + y^2 + (z - z_0)^2} \tag{35}$$

As previously mentioned, the temperature gradient outlines clearly show the effect of the heat source summation. For Gaussians distant from each other, the total source impact is diminished, leading to maximum temperature around 17°C, whereas for distribution centred closer to z_0=0 mm, the effect is largely perceivable, causing temperature gradients around 45°C. Naturally, for positions further form the z-axis, the impact will be smaller due to the source volumetric response, which is larger closer to the source.

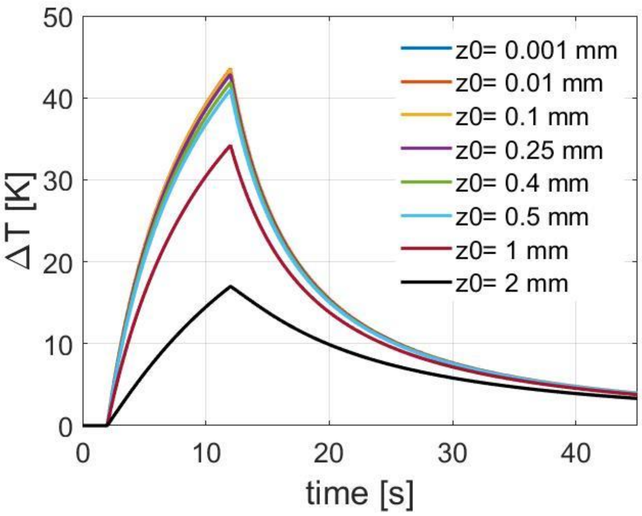

Figure 8.5- *z0 comparison temperature evaluations.*

Figure 8.5 describes the temperature gradient profiles obtained varying the positions of the two source functions summed. Evident is the effect of the function definition as explained above. The latter has huge impact from z_0=2 mm to 1 mm, whereas it decreases from z_0= 0.25 mm on, where convergence is reached, and the maximum temperature gradients obtained is stabilized.

Lastly, a simulation considering the heat source as the summation of some of the previously functions was performed. The analysis was made with Gaussians centred at z_0= [0.1, 0.25, 0.5, 1, 2] mm and their negative corresponding. The power carried by each Gaussian was set equal to 0.1667.

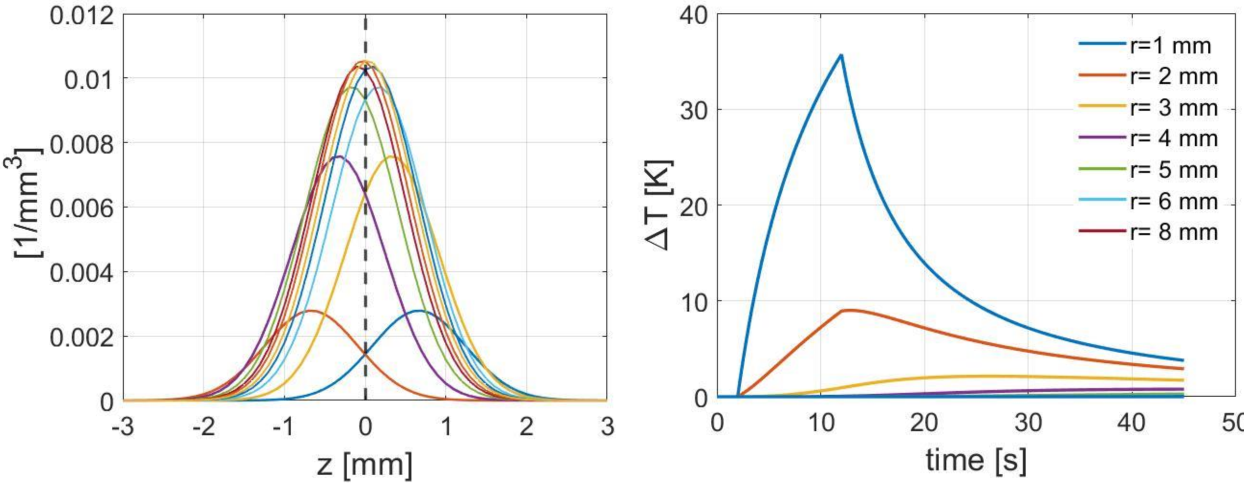

Figure 6- *Heat source as sum of 10 gaussians differently centred. Temperature effect of the source.*

Figure 8.6 portrays the summation of the ten considered Gaussian functions and their effect over the volumetric domain, leading to temperature gradients along the media positions that respect the average values retrieved from all other simulations. The maximum temperature obtained is 35.7°C.

8.4 Comsol delivery system analysis

In order to recreate the most possible realistic delivery system, a new analysis was carried out through CM software. The main objective was to mathematically describe a Gaussian function with standard variation increasing linearly over the z-axis and power decreasing exponentially along the vertical direction.

Following these indications, a mathematical analysis was performed, and a new volume source formulation was adopted:

$$p(z) = p_0 e^{-\lambda z} \tag{36}$$

$p(z)$ [W/m], describes the exponential power evolution along the z-axis, as visible in Figure 8.7.

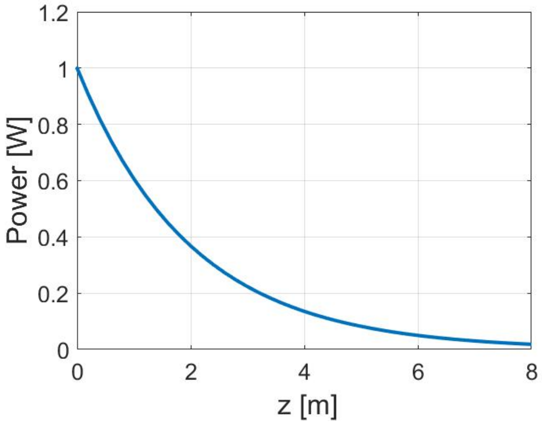

Figure 8.*7- Power variation along z-axis.*

Integrating Equation 36 over the domain we obtain the total power which can be later exploited for the computation of the heat source desired.

$$\int_0^{+\infty} p(z)\,dz = q \tag{37}$$

$$\frac{p_0}{\lambda} = q \tag{38}$$

$$p_0 = q\lambda \tag{39}$$

$$Q(x,y,z) = \begin{cases} 0, & z < 0 \\ \dfrac{q\lambda}{2\pi\sigma^2(z)} \cdot exp\left(-\dfrac{r^2}{2\sigma^2(z)}\right), & z \geq 0 \end{cases} \tag{40}$$

$$\sigma(z) = a + b \cdot z \tag{41}$$

Where $Q(x, y, z)$ represent the volumetric Gaussian distribution, with power exponentially varying along the z-axis (Equation 36).

As previously stated, the standard variation (σ) changes linearly along z-axis, starting from a preset value a of 0.1 mm. b instead expresses the slope of the standard deviation variation, a fundamental parameter which has been thoroughly investigated in the subsequent simulations. The absorption length λ [1/m] is another important parameter later studied since it largely influences the source propagation as visible in Figure 8.8.

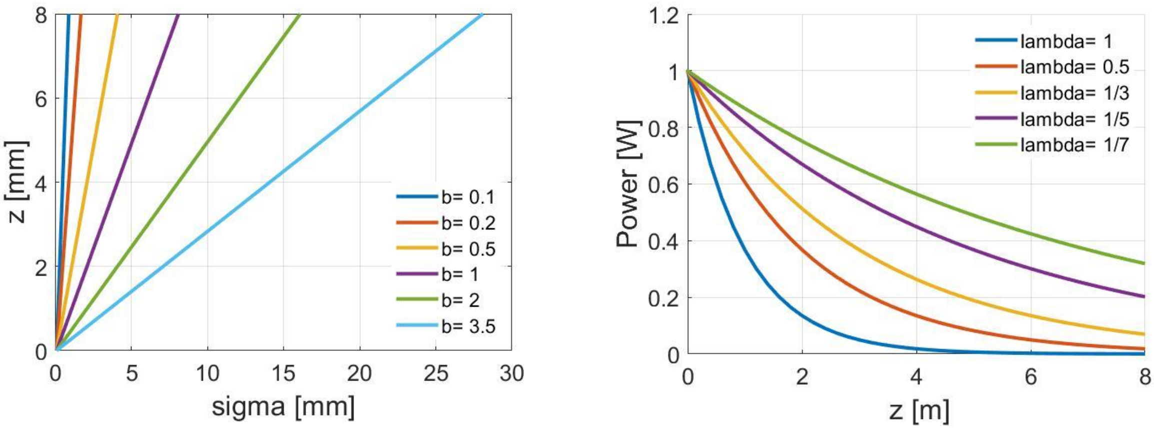

***Figure 8.8**- Standard deviation variation along z-axis and Power variation along z varying λ.*

Depending on b and λ entity, the cone laser emission deeply changes. Simulations implementing the above equations were performed changing b constant value from 3.5 to 0.1 and λ values from 2 to 0.143 [1/mm]. The overall power was set as for the previous simulation equal to 1 W, with heat source activated at 2 s and stopped at 12 s.

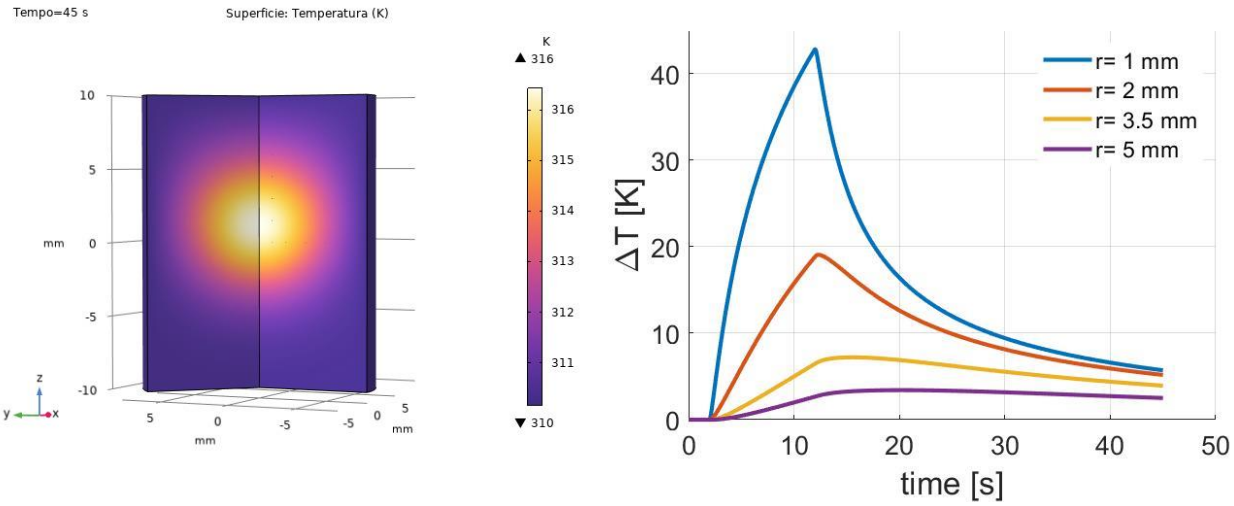

Figure 8.9- *Temperature gradient evaluations for $\lambda = 1$ and b= 3.*

Figure 8.9 portrays the temperature gradient responses to the heat source defined setting λ and b equal to 1 and 3 respectively. Firstly, Figure 8.9 on the left, which depicts the volumetric temperature gradient, verifies the correctness of the model implemented since it is clearly visible the heat source impact, which is applied for $z \geq 0$.

Generally, this situation, has been considered as a reference setting for this delivery system study since the values obtained fit exactly the ones retrieved with a standard heat source, thus, all previous simulations.

At this point, interesting was investigating the impact of the two parameters above described. The analysis was conducted establishing one parameter values as reference one, i.e either b =3 or λ =1 [1/mm], and changing the other based on the previously described ranges. Figures 8.10, 8.11 show the temperature gradients observed along z-axis varying the standard deviation definition and the absorption coefficient.

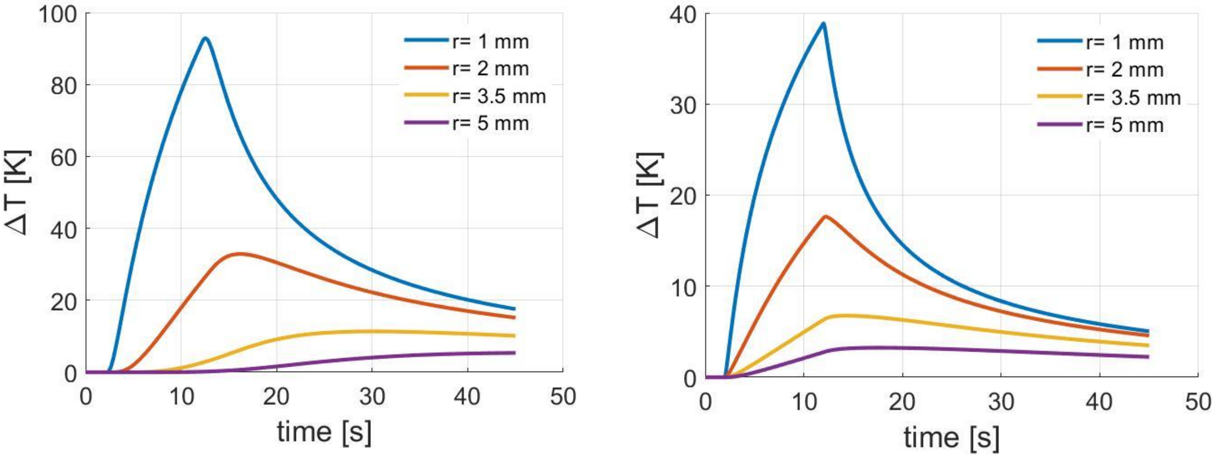

Figure 8.10*- Radial temperature outlines limit cases. b= 0.1 and b=3.5.*

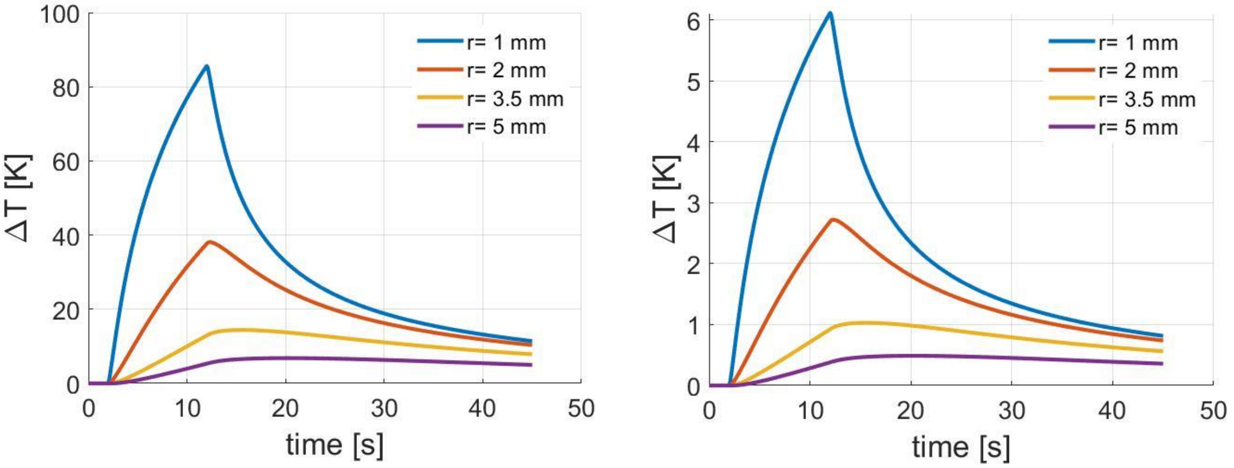

Figure 8.11- *Radial temperature outlines limit cases. λ = 0.5 and λ =1/7.*

Interesting is observing the huge impact of the radiation cone characteristic as well as the absorption length. With low *b* values, temperature reaches up to 93 C, whilst for high λ's, the highest temperature retrieved is 86 C.

These two limit conditions would induce cell necrosis, which is the main objective of the laser ablation therapy.

However, since the temperature range obtained is huge, no reliability can be conferred to the model. Compelling was nonetheless obtaining results physically reasonable respect to the characteristics of the power emission. In theory indeed, by increasing the range of radiation propagation, a lower power density will be present and general decrease of the entity of the temperature response is expected. The same is foreseeable considering high power absorption length. High values of λ lead to high heat absorption close to the source, provoking larger temperature gradients.

The more realistic scenarios, described by b between 2 and 3 and λ between 1 and 1/3 [1/mm] for example, respects the predicted value ranges.

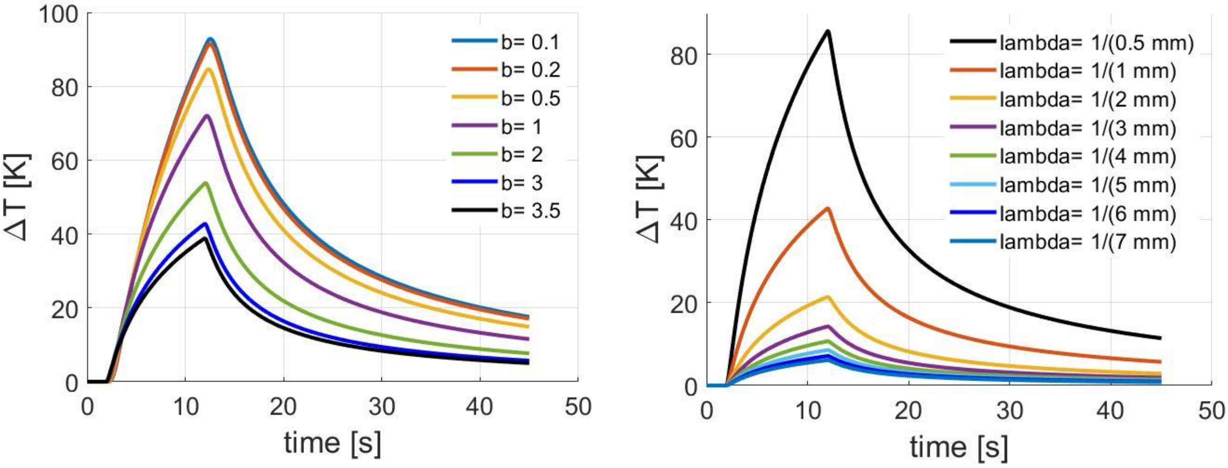

***Figure 8.12**- Comparison of temperature observed at r= 1mm, varying b and λ.*

Figure 8.12 highlights the huge impact of the heat propagation over the temperature evaluations at r= 1 mm. The slope of the increasing Gaussian standard deviation and the entity of exponential power decay are indeed fundamental to comprehend the thermal media response. Between b= 0.1 and b= 3.5, differences on the order of 60°C are presents, whereas between λ= 2 and λ= 0.143 [1/mm], the discrepancies are on the order of 80°C. From a technological point of view these results do not allow the building of a reliable mock-up for treatment measurement analysis.

Part IV

Experimental activities

Chapter 9

9.1 Introduction

Experiments have been conducted to validate the CM mock-up model.

The impact of glass and the presence of air inside the fibre setting during the simulation was first examined, since a quick rise in temperature behaviour was witnessed at r= 1 mm from the source. Afterwards, a check on the numerical solutions found in the 2D axial symmetric model was conducted.

Hence, real temperature monitoring was performed using MicronOptics technology, a built mock-up, and a laser beam, which was firstly characterised and then controlled by LabVIEW® software.

9.2 Used instrumentations

The equipment involved in the thermal treatment test are two: one generates and administer the laser beam, whereas the other device measures the media temperature response. Two laser devices were utilised, each one based on a laser diode and controlled by a LabVIEW® program that allows the setting and the control of laser beam parameters, as well as data acquisitions from Micron Optic device. As visible in Figure 9.1, the two systems are thus controlled by two buttons on a LabVIEW® program, that enable the turning of the irradiation and the data acquisitions with perfect synchronization. This optimal experimental set-up was achieved thanks to a relè connected to the Laser that controls its ON/OFF setting. The emission wavelength of the two lasers employed are 915 nm and 1470 nm, both in a continuous wave modality. Fig. 9.1 shows the user interface in LabVIEW.

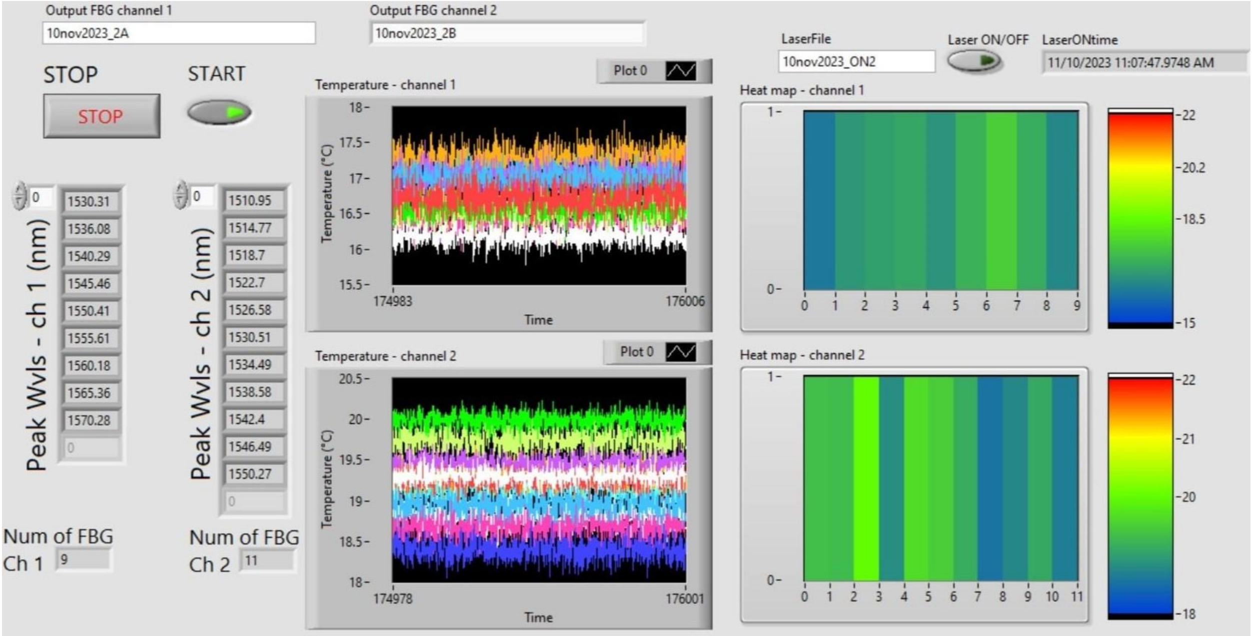

Output FBG channel 1
10nov2023_2A

Output FBG channel 2
10nov2023_2B

LaserFile
10nov2023_ON2

LaserONtime
11/10/2023 11:07:47.9748 AM

Peak Wvls - ch 1 (nm)
0
1530.31
1536.08
1540.29
1545.46
1550.41
1555.61
1560.18
1565.36
1570.28
0

Peak Wvls - ch 2 (nm)
0
1510.95
1514.77
1518.7
1522.7
1526.58
1530.51
1534.49
1538.58
1542.4
1546.49
1550.27
0

Num of FBG Ch 1: 9

Num of FBG Ch 2: 11

Figure 9.1- *Labview- operator interface.*

To accurately depict the temperature range distribution surrounding the exposed area, we used a multi-point FBG sensor in the experimental experiments. Thus, two crossed optical fibre arrays for acquisitions, placed in the domain's centre, served as the foundation of the monitoring system. Two single-mode fibres with nine (horizontal) and eleven (vertical) FBGs were utilised; characterized by a core diameter of 9 µm and a cladding diameter of 125 µm. The FBG interrogation device's communication and data transmission are managed by a LabVIEW programme. The

Micron Optics HYPERION si155 FBG interrogator enables simultaneous acquisition for experimental testing.

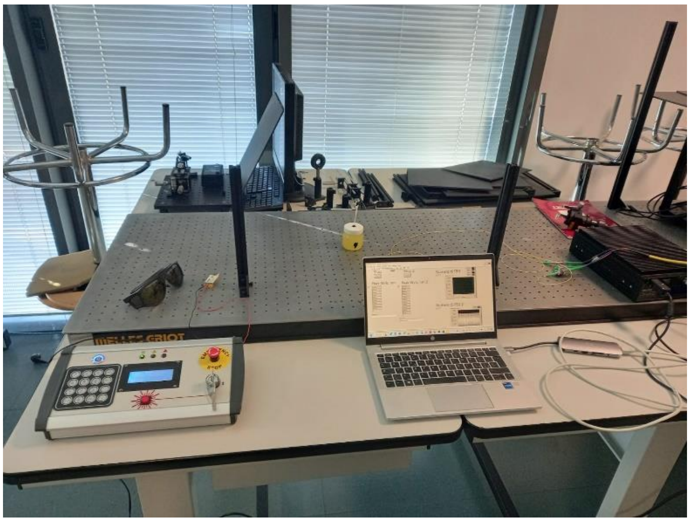

Figure 9.2- General experimental simulation set-up.

9.3 Bragg wavelength

A text file contains the Bragg wavelength peaks that Micron Optics recorded for every channel. The following relation allows us to extract the corresponding temperatures through the attained wavelengths:

$$\Delta T = \frac{\lambda_B - \lambda_0}{K_0} \tag{42}$$

where λ_0 is the initial value of Bragg wavelength acquired by the optical interrogator at the beginning of the test, defined through a specific calibration that allows the computation of the temperature sensitivity coefficient K_0, required by the LabVIEW program before data acquisition. After calibration, conducted considering an initial temperature of 20°C, K_0 was set equal to 10 picometres per degree Celsius.

9.3 Phantom

As visible in Figure 9.23, a phantom was constructed to carry out experimental simulations, which are required to verify numerical solutions found previously.

The aim was to generate a phantom with conditions as close as possible to the CM model. Thus, inside a yoghurt plastic container, vertical and horizontal arrays were placed and secured using silicone. They were both implanted in glass coatings of 0.25 mm thickness and 1 mm diameter to examine the temperature distortions that were previously established in Chapter 7. They are characterized by 9 and 11 reticula respectively. Phantom dimensions are thought to have no influence over the recovered temperatures since they are far bigger than the limit values determined in Chapter 4, with lengths on the order of few millimetres (L1=2 mm).

The optical fiber, connected to the Laser, was finally positioned at the centre of the domain by inserting it in a vertical glass coating, with 1 mm diameter and a coating of 0.25 mm thickness too, fixed at 1 mm far from the monitoring system. The phantom was designed in the described way to guarantee the desired separation between the delivery and the sensing system.

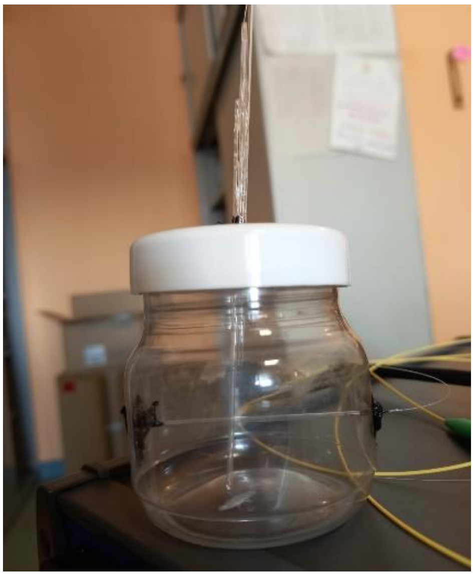

Figure 9.3- Built phantom.

The choice of the medium was Agar, a jelly-like substance consisting of polysaccharides mixed with water to obtain a solid model, and egg white, due to its high-water concentration. Egg white is indeed made of:

- 88% of water
- 11% of proteins

The rest 11% is made of various lipids and carbohydrates. Generally, egg white properties are similar to water ones. Furthermore, the chosen media can be considered an excellent choice since most of the human organs are made of water and egg white reliably represent the venous system present in them.

To enhance the absorption length of the Agar, generally too small compared to the human tissue ones, ink was diluted inside it during the cooking process.

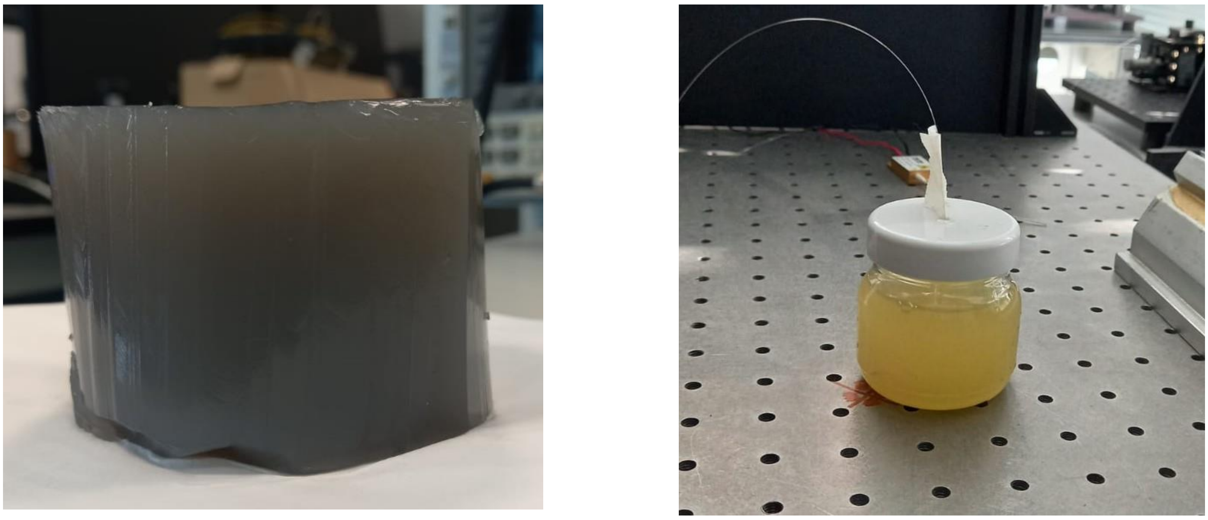

Figure 9.4- *Agar volume and Egg- white chosen for the experimental simulations.*

After instrumentation’s characterization, simulations were performed considering heating and cooling transients, varying the total power induced.

9.4 Experimental Results

The experimental session was conducted employing a 950 nm laser. After data postprocessing, ulterior simulations were performed with the 1470 nm one, in order to achieve better thermal responses.

At first, FBGs and Laser characterization was necessary to retrieve reliable values. Evaluations of λ_0 Bragg initial wavelength and Laser real output power were indeed assessed. Power losses resulting from fibre splicing were identified prior to conducting heating testing.

Sessions were run as follows:

- Wavelength data acquisition with no source for unspecified time;
- Activation of Laser for 10 seconds, as done for CM software simulations;
- Analysis of the cooling transient: wavelength acquisition stopped once temperature values became stable;
- Team reasoning and post processing.

Equation 42 was utilised to obtain all temperature gradients from MicronOptics wavelength acquisitions.

Figure 9.5 shows the thermal response of the egg-white to a 950 nm Laser at different powers along the vertical direction.

The temperature trends respect the source applied. Nonetheless the heat absorption, thus temperature rise, is mere compared to the numerical solution previously found, i.e. evaporation for power > 3 W.

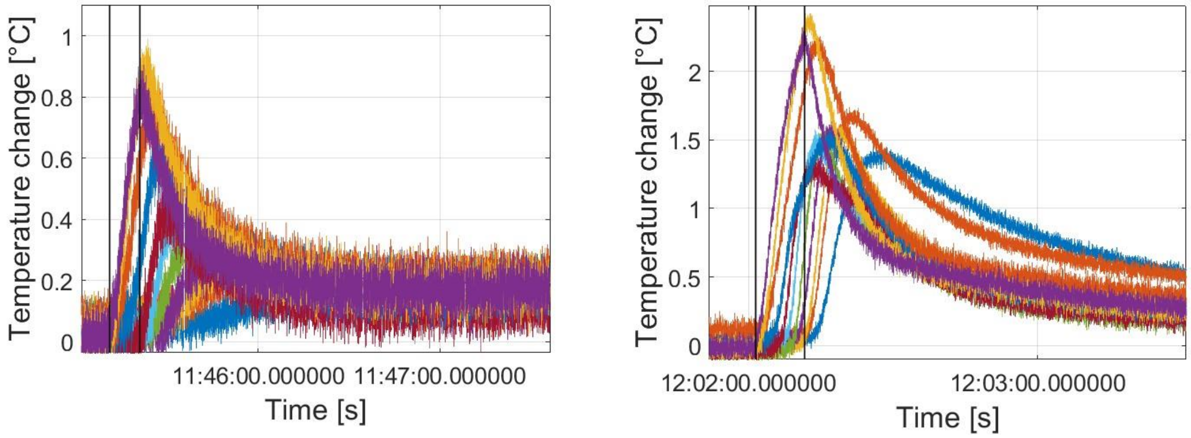

Figure 9.5-*Temperature gradients. Egg-white, WL 950 nm. Power: (3.3 and 12.6) W.*

Figure 9.6 below explicit the Agar temperature gradients obtained as a result of the application of a 950 nm laser. As for the egg white, the retrieved values are lower than expected, despite being higher than the egg white simulations. These results allowed to comprehend that Agar, mixed with ink, is characterized by higher radiation absorption length respect to the egg white, possibly because of its thermal properties, like density (inversely proportional to ΔT):

- *1040 kg/m*^{3} Eggwhite
- *550 kg/m*^{3} Agar

Furthermore, the low temperature gradients obtained was considered to be the effect of Laser characteristic, i.e. low wavelengths.

Hence, new experiments were carried out employing a 1470 nm Laser.

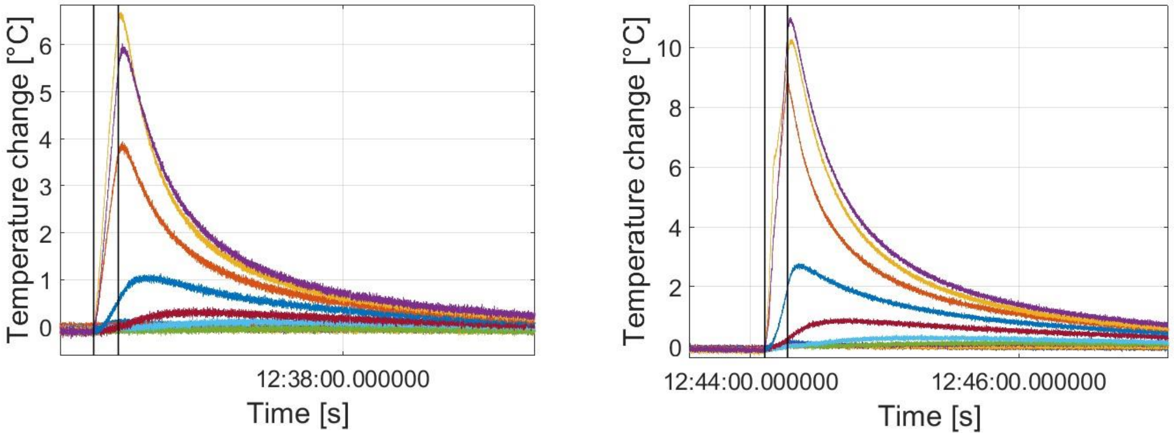

Figure 9.6*-Temperature gradients. Agar, WL 950 nm. Power: (3.3 and 7.6) W.*

As clearly visible in Figure 9.7 and 9.9, the Laser largely impact the thermal responses of both phantoms.

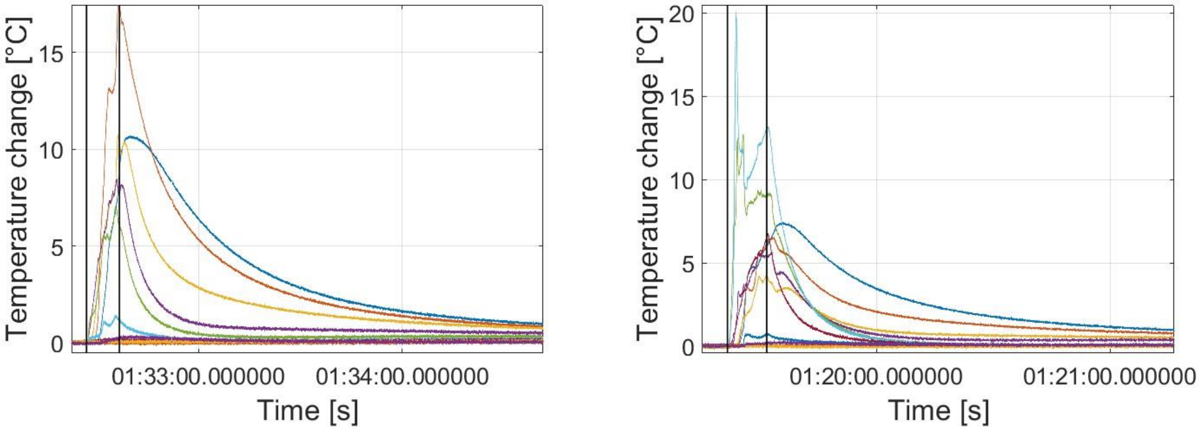

Figure 9.*7-Temperature gradients. Egg-white, WL 1470 nm. Power: (2.21 and 3.3) W.*

For the Egg white, even for low power values, maximum temperature between 15°C and 20°C are reached. Egg coagulation occurs around the tip of the optical fiber, as highlighted by Figure 9.8.

Figure 9.8- *Egg coagulation for 2.21 W power.*

Temperature gradients comparable to the numerical solution found both analytically and on CM can be witnessed in Figure 9.9, where a maximum temperature gradient of 47.7°C is found on the central FBG of the vertical array, immerged in the Agar volume.

The maximum temperature gradient obtained in the analytical solution at 1 mm from the source, was around 41°C for 1 W power output.

The discrepancies between the numerical solution and the experimental one could be caused by lots of factors, analysed carefully throughout the master thesis, such as: heat source definition, power absorption length, material thermal properties etc…

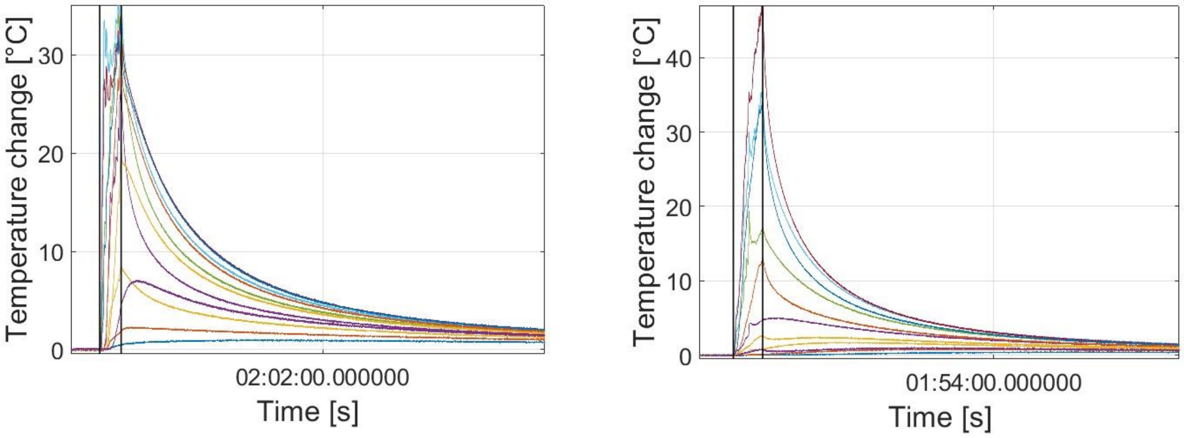

Figure 9.9*-Temperature gradients. Egg-white, WL 1470 nm. Power: (2.21 and 3.3)W.*

Almost equal behaviour was indeed found by employing as source Equation 40, with *b*= 3 and *λ*= 1/2 [1/mm] and power equal to 3.3 W. (Figure 9.10)

In this case, the maximum temperature retrieved at r= 1 mm and z= 0 mm, is equal to 47.4°C, with 0.3°C discrepancies from the experimental solution.

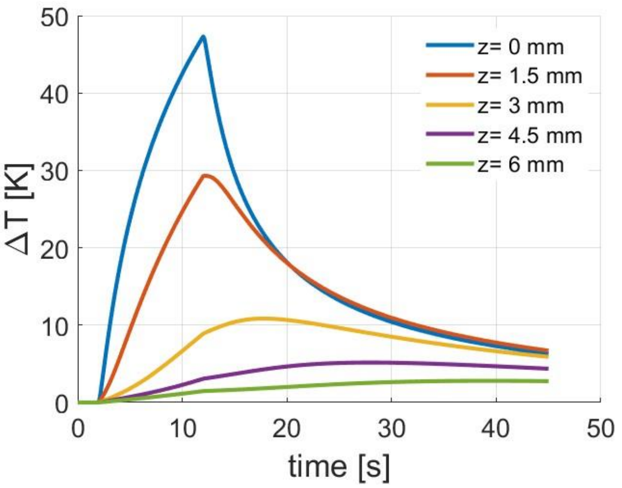

Figure 9.10*- Temperature gradients. Source defined as Eq.40 with b=3 and λ =1/(2mm).*

In conclusion, the model implemented can be considered correct despite the monitoring fiber coating impact found in the numerical simulations, is evidently not present.

Eventually, an analysis over the temperature trend further in time was performed. The objective was to verify the exponential temperature decay that manifests in the analytical solution.

Figure 9.11 depicts the situation just described. During cooling down phase, the temperatures slowly decrease following and exponential evolution.

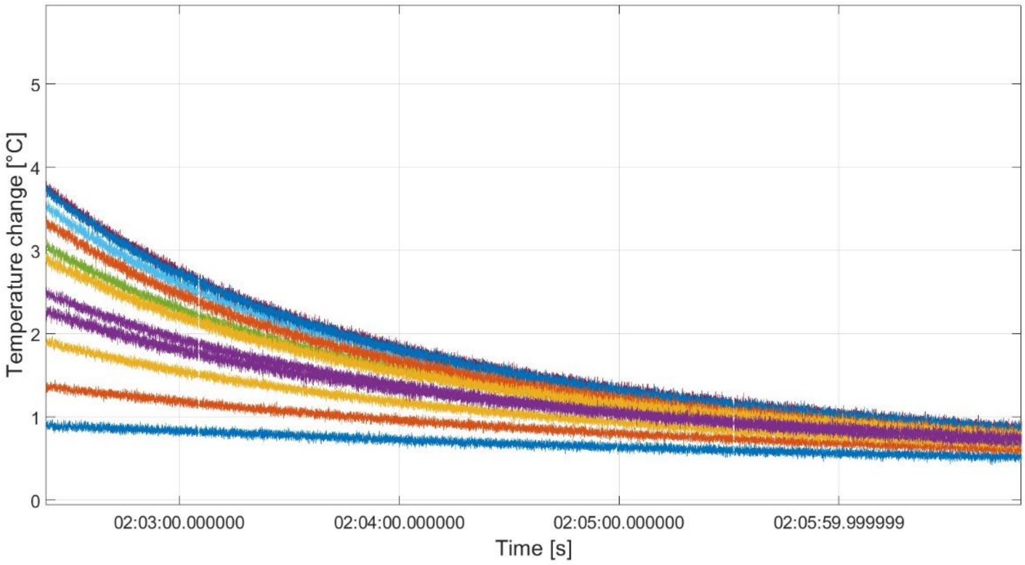

Figure 9.11- *Exponential behaviour of the temperature as theory foresees.*

Part V

Conclusions

Chapter 10

Conclusions and future outlooks

Cancer is still a global public health issue in 2023. However new research and techniques for treatment purposes have been constantly developed during the last few years, increasing the overall survival rate.

Interested in minimally invasive approaches has growth significantly over the medical personnel due to their high accuracies and low invasiveness over the patient during treatment.

The examination of laser ablation, a minimally invasive thermal treatment that causes cell necrosis by depositing heat on biological tissue, was the main subject of this master's thesis project.

The conducted study set out to examine, forecast, and quantify laser-tissue interactions to provide the medical staff a trustworthy mock-up for treatment planning.

A realistic model was constructed on the Comsol Multiphysics software, able to solve numerically the bio-heat equation, to assess the thermal response over time induced by a laser impulse along the medium volume. Water was chosen as material for the mock-up due to properties similarity with the liver, chosen as reference human organ. The retrieved thermal response was then compared to the analytical solution to verify the correctness of the model and to understand the limitations of the built model over the theorical solution obtained supposing an infinite medium.

Heat pulse method was then employed to obtain a map of the realistic thermal properties of the model, necessary for determining accurate heat distributions across the media.

During the thesis work, huge attention has then been put into the monitoring system definition and delivery system characterization.

Previous studies showed that conventional polymer fiber coatings were too susceptible to strain and temperature deformations. Hence, glass embeddings, despite their high thermal inertias, were chosen to obtain less influenced acquisitions.

Analysis of the induced distortions in the temperature maps was thus carried out.

In contrast to expectations, the air volume between the glass coating, the glass core of the monitoring fibre, and the monitoring fibre itself all had a significant impact on the retrieved readings. Differences of almost 70°C were found at a distance of 1 mm from the heat source. These measurements indicate significant temperature overestimations and, for the most part, potentially dangerous incorrect medical assessments: cell necrosis is believed to have accomplished, although actual temperature gradients demonstrate insufficient thermal stress to cause malignant cell damage.

To gain a deeper understanding of the peculiar outcomes, experiments have been carried out. A laser with varying power settings was used to irradiate a phantom that was constructed approximating the CM model as closely as possible. The Micron Optic device, which was linked to two crossed FBG arrays inserted into glass coatings as simulated by the aforementioned programme, was used to acquire the temperature responses. Because egg white has a high-water content and resembles the venous system in the human body, it was chosen as the material for the study. Other experiments were performed also employing a cylindrical Agar phantom.

The obtained results showed that the implemented model can be evaluated as correct. Agar phantom, which is the closest one respect to the one employed in the CM analysis, indeed showed thermal behaviour comparable to the one obtained analysing the system delivery (see below). Nonetheless, the huge fiber impact over the temperature maps found before, did not present itself throughout the experimental session.

Eventually, a thorough investigation was performed on the emission source definition, to better resemble real scenario laser devices. Heat equation linearity was exploited to define the source as a summation of multiple Gaussians. Firstly, through Matlab software, summation varying the starting position of the source emission was performed. Outcomes were consistent with expectations, resulting in average temperature readings that matched the previously discovered numerical values.

Then, a more precise description was given, accounting the power decay along the application direction and the heat source cone emission. The power was thus defined as exponentially declining along the z-axis, while the Gaussian standard deviation was increased along the same axis.

Temperature outlines obtained showed huge influences of some fundamental source definition parameters over the data acquisitioned. The rate of power decay, as well as the geometric radiation propagation, distort the temperature outcomes leading to either underestimations on the order of 35°C, or overestimation on the order of 50°C respectively, making the defined mock-up still unreliable for medical treatment plannings.

However, the observed thermal responses manifestly adhere to physical logic; the retrieved temperature gradients fit the one obtained with simplified source definition and the analytical solution when realistic heat source parameters were set.

Obviously, there are still a lot of future improvements that can be accomplished to the measurement’s organisation as well as the model. Subsequent investigations may concentrate on improving the accuracy of the source definition by examining the optical interaction between the biological tissue and the laser, with emphasis on the percentage of light that is absorbed and scattered over the total given.

Increased attention should also be paid to the definitions of the medium parameters, such as thermal conductivity, absorption coefficient, and scattering coefficient, which should be incorporated into the model as temperature-varying functions rather than constant values, as observed in real-world scenarios. Additionally, the aforementioned criteria differ between tissues that are malignant and those that are not. Thus, it would be possible to apply differentiated models that interact continuously to identify differences between the two scenarios under analysis.

The application of the model to heterogeneous tissues, including in vivo ones, might also be investigated.

It may be interesting to account for the biological organ properties such as arterial blood temperature, blood specific heat, perfusion index, density, and metabolic source, that are essential to Penne's heat equation but are here disregarded.

Studying the fibre shadow effect, which appears when numerous fibres are considered, would be interesting too.

Finally, by monitoring fibre distortion and defining the thermal source, this master's thesis helped to understand the key concerns surrounding the construction of a trustworthy and realistic mock-up for treatment planning. These findings can serve as a foundation for further research.

References

[1] Akbar Basha Shaik, Penchalaiah Palla. «Optical quantum technologies with hexagonal boron nitride single photon sources.» June 2021. (pag 29)

[2] American Cancer Society. «Cancer Facts & Figures.» 2023. *Less invasive Cancer surgey techniques.* 2 october 2019. https://www.cancer.org/cancer/managing-cancer/treatment-types/surgery/special-surgical-techniques.html. (Pag 10-12)

[3] Amira S. Ashour, Yanhui Guo, Waleed S. Mohamed. «Mathematics and finite element method of thermal ablation therapy.» *Academic Press*, 2021. (pag 43-46)

[4] BALLARAT SKIN CARE CENTER. *Micrographic surgery.* s.d. https://ballaratskincancer.com.au/micrographic-surgery/. (pag 23)

[5] Cleveland Clinic. *Liver Cancer.* s.d. https://my.clevelandclinic.org/health/diseases/9418-liver-cancer. (pag 13)

[6] Comsol Multiphysics. «The Finite Element Method (FEM).» *COMSOL.* 15 March 2016. https://www.comsol.it/multiphysics/finite-element-method. (pag 59-61)

[7] ELECTRONICS| PROJECTS| FOCUS. «Laser Diode Operation and Its Applications.» *ELECTRONICS| PROJECTS| FOCUS.* s.d. https://www.elprocus.com/laser-diode-construction-working-applications/. (pag 32)

[8] Emiliano Schena, Paola Saccomandi, and Yuman Fong. «Laser Ablation for Cancer: Past, Present and Future.» *NIH, National library of Medicine*, 14 June 2017. (pag 19)

[9] FBGS. «FemtoSecond Gratings (FSG®).» *FBGS.* s.d. https://fbgs.com/components/femtosecond-gratings-fsg/. (pag 37-38)

[10] Fundamentals of Fiber Optics . «Basic Structure of an Optical Fiber.» *Fundamentals of Fiber Optics* . s.d. https://mypdh.engineer/lessons/basic-structure-of-an-optical-fiber/. (pag 33-36)

[11] Haemmerich, Dieter. «Mathematical modeling of heat transfer in biological tissues (bioheat transfer).» *Accademic Press*, 2022.

[12] kik, Tomasz. «Heat Source Models in Numerical Simulations of Laser Welding.» *MDPI,* 10 june 2020. (pag 66-67)

[13] Life of Physics. «RUBY LASER , construction, working,Advantage, Disadvantage, Application.» *Life of Physics.* s.d. https://learnfuturephysics.blogspot.com/2017/08/ruby-laser-construction.html. (pag 28)

[14] MacMillan cancer support. *Rare cancers.* 1 november 2019. https://www.macmillan.org.uk/cancer-information-and-support/rare-cancers. (pag 12)

[15] Mayo Clinic . *Stereotactic radiosurgery.* 7 April 2019. https://www.mayoclinic.org/tests-procedures/stereotactic-radiosurgery/about/pac-20384526. (pag 24-25)

[16] Meghan G. Lubner, MD, PhD Christopher L Brace, e MD and Fred T. Lee, Jr., MD J. Louis Hinshaw. «Microwave Tumor Ablation: Mechanism of Action, Clinical Results and Devices.» *NIH, National Library of Medicine*, 11 August 2011. (Pag 17-18)

[17] Miao Lin, Pat Eiken and Shanda Blackmon. «Image guided thermal ablation in lung cancer treatment.» *Journal of Thoracic Disease*, November 12, 2020.

[18] Mini Physics. «Total Internal Reflection.» *Mini Physics.* 25 December 2015. https://www.miniphysics.com/total-internal-reflection-2.html. (pag 34)

[19] Mohammad Ali Ansari, Mohsen Erfanzadeh, and Ezeddin Mohajerani. *Mechanisms of Laser-Tissue Interaction: II. Tissue Thermal Properties.* J Lasers Med Sci., 2013 . (pag 40-42)

[20] Munde, Dr. Yadav. *Radiofrequency Ablation (RFA) of various Tumours.* s.d. https://dryadavmunde.com/radiofrequency-ablation-rfa-of-various-tumours/. (pag 16-17)

[21] NIH, national cancer institute. *Types of cancer treatments.* s.d. https://www.cancer.gov/about-cancer/treatment/types. (pag 12)

[22] Orsetti, Rosita. «Model-based planning and real time monitorino for laser thermal theraphy in ophthalmology .» Master's Thesis, Torino, 2022. (pag 55)

[23] Physics and Radio electronics. «Methods of Achieving Population Inversion.» *Physics and Radio electronics.* s.d. https://www.physics-and-radio-electronics.com/physics/laser/methodsofachievingpopulationinversion.html#google_vignette. (pag 30)

[24] Rebecca L. Siegel MPH, Kimberly D. Miller MPH, Nikita Sandeep Wagle MBBS, MHA, PhD, Ahmedin Jemal DVM, PhD. «Cancer statistics, 2023.» *ACS journals*, 12 January 2023: 5-15. (pag 11)

[25] scaime. *Fibre Bragg grating sensor technology.* s.d. https://scaime.com/fibre-bragg-grating-technology. (pag 36-38)

[26] Simpson, Dr Emily. «The Basic Principles Of Laser Technology, Uses And Safety Measures In Anaesthesia.» *WFSA.* 19 march 2012. paghttps://resources.wfsahq.org/atotw/the-basic-principles-of-laser-

technology-uses-and-safety-measures-in-anaesthesia/#:~:text=Laser%20is%20produced%20by%20the,order%20to%20exert%20biological%20effect. (pag 27-31)

[27] Supino, Armando. «Sviluppo di modelli termici per l'ablazione laser di tumori.» Master's Thesis, Torino, 2022.

[28] Team Xometry. «Diode Lasers: Definition, How They Work, Types, Applications, and How to Use.» *Xometry.* 17 June 2023. https://www.xometry.com/resources/sheet/diode-lasers/#:~:text=Diode%20lasers%20work%20by%20stimulating,and%20amplification%20of%20coherent%20light. (pag 32-33)

[29] Tzure, Tlalit Bussi Tel. «World Cancer Day: How Minimally Invasive Treatments Can Be Leveraged To Reach Underserved Populations.» *Forbes*, Feb 3, 2023. (pag 15)

[30] UICC. «Global Cancer Data: GLOBOCAN 2018.» september 12, 2018. (pag 10)

[31] USGS: science for a changing world. *The water in you: Water and the human body.* 22 may 2019. https://www.usgs.gov/special-topics/water-science-school/science/water-you-water-and-human-body#:~:text=Up%20to%2060%25%20of%20the,bones%20are%20watery%3A%2031%25. (pag 64).

[32] Wai-ki Yiu, MBBS MRCS,1,2 Maria T Basco, MD,1 John E Aruny, MD, Stephen WK Cheng, MS FRCS FACS, and Bauer E Sumpio, MD PhD FICA. «Cryosurgery: A review.» *NIH, National library of Medicine* , 2007. (pag 20)

[33] Wolfran Mathworld. *Green's Function.* s.d. https://mathworld.wolfram.com/GreensFunction.html#:~:text=Generally%20

speaking%2C%20a%20Green's%20function,examples%20such%20as%20in homogeneous%20partial. (pag 46)

[34] Yi-Hsuan Hsiao, Shou-Jen Kuo, Horng-Der Tsai, Ming-Chih Chou, and Guang-Perng Yeh. «Clinical Application of High-intensity Focused Ultrasound in Cancer Therapy.» *NIH, National Library of Medicine*, 3 Jan 2003. (pag 21)

[35] Yüksel, Numan. «The Review of Some Commonly Used Methods and Techniques to Measure the Thermal Conductivity of Insulation Materials.» *CHAPTER METRICS OVERVIEW*, 31 August 2016. (pag 50-54)